*Preliminary*

# The Divertor Program in Stellarators

R. König[1], P.Grigull[2], K. McCormick[2], Y. Feng[2], J. Kisslinger[2], A. Komori[4],
S. Masuzaki[4], K. Matsuoka[4], T. Obiki[3], N. Ohyabu[4], H. Renner[1],
F. Sardei[2], F. Wagner[1], A. Werner[2]

[1]*Max-Planck-Institute for Plasma Physics,Garching, EURATOM Ass., D-17491 Greifswald, Germany*
[2]*Max-Planck-Institute for Plasma Physics,Garching, EURATOM Ass., D-85748 Garching, Germany*
[3]*Institute of Advanced Energy, Kyoto University, Gakasho, Uji, Japan*
[4]*National Institute for Fusion Science, Toki-shi, Gifu-ken 509-5292, Japan*

**Abstract.** With LHD and W7-X the stellarator development is now taking a large leap forward on the path to a steady-state fusion reactor. Important issues that need to be settled in these machines are the particle and heat control, and the impact of divertors on plasma performance in future continuously burning fusion plasmas. The different paths initially followed in these stellarators were carefully prepared in smaller scale devices like Heliotron E, CHS and W7-AS. While advanced divertor scenarios relevant for W7-X are still being explored on W7-AS for another year, other smaller scale experiments like Heliotron-J and CHS will be used for the further development of divertor concepts and could thereby nourish later divertor generations of the two large machines. Two types of divertor configurations are presently being investigated, the helical and the island divertor (including the Local Island Divertor (LID)). The LID concept, following its successful demonstration on CHS, will be available on LHD from 2002 onward. In designing LHD, careful consideration was given to the realisation of a helical divertor, the basic function of which had already been studied in Heliotron-E. First experiments in LHD performed in an open helical divertor configuration are being followed by experiments with a local helical divertor on the route to a closed full helical divertor. Owing to the flexibility of the field configuration control in Heliotron-J comparative studies of helical and island divertors will be performed in this machine in phase II from 2003 onward. On W7-X an actively cooled discrete island divertor (10 modules) will be installed. This development is preceded by extensive investigations into the island divertor concept over many years now, experimentally as well as theoretically by 3-D modelling, and culminated in the first installation of a discrete island divertor, very similar to the one planned for W7-X, on W7-AS last year. The first experiments with this newly installed open island divertor opened a window to a completely new ultra high density (UHD) operating regime. At high NBI power (up to 2 MW) line averaged densities of up to $3 \cdot 10^{20}$ m$^{-3}$ were for the first time reached in a controlled and quasi stationary way. Without divertor these discharges ran into a density limit and terminated in a radiative collapse after about 200-300 ms, while now, with divertor, one no longer looses density control and no radiation problem arises. While the edge strongly radiates, the core radiation stays low throughout the entire discharge. The radiation level remained stationary up to the maximum discharge length of presently 1 sec without any sign of limitations while the impurity confinement time falls sharply with increasing line averaged density up to the maximum density so far explored ($3.5 \cdot 10^{20}$ m$^{-3}$). Ramping up density from $1.5 \cdot 10^{20}$ m$^{-3}$ to higher values, leads to stationary local partial detachment at radiation levels of 70-80% of the absorbed neutral beam power . The radiation was concentrated near the x-points. The emerging radiative mantle has some resemblance with the TEXTOR RI-mode but with the advantage that, while in TEXTOR the plasma detaches from the limiter, in W7-AS the plasma partially detaches at the watershed, but remains attached in other locations on the divertor target. The partial detachment presumably helps to stabilise the position of the radiation layer. A corollary of this is maintenance of high neutral gas pressure in the divertor in the $10^{-3}$ mbar region, which will allow high neutral pumping via titanium gettering in the divertor sub-volume later in the program. Considerable efforts have been invested into the development of the 3-D transport code EMC3/EIRENE which

recently has been extended to handle arbitrary ergodic boundaries by using a new reversible field-line mapping (RFLM) technique. First comparisons with the latest divertor experiments have shown excellent agreement. They have particularly proven the code prediction that sufficiently high momentum losses to reach detachment are provided by cross-field transport associated with the particular island divertor geometry, thereby giving access to detachment without going through a high recycling phase, a unique feature of the island divertor geometry.

## 1.     Introduction

Two significant problems that need to be solved for any fusion system and which are intimately connected with the plasma edge, are heat removal and particle control. A very promising method to attack these problems in tokamaks and helical devices, is the use of a divertor, providing a controlled interaction zone between plasma and wall. It is believed and has partly been shown already, that by carefully designing a divertor, conditions can be created in front of  the divertor targets, which lead to a sufficient reduction of the power load on the targets by strong radiation redistribution. Any solution of course needs to allow for an energy confinement which is at least sufficient for the realisation of a fusion reactor. Since energy confinement  has been found to be strongly related to edge anomalous transport and edge plasma profiles, the ultimate aim of course is to find an integral solution which is optimum in respect to exhaust, heat load and energy confinement.

Two main types of configurations are proposed for a divertor in a helical device: the 'helical divertor' and the 'island divertor'. So far divertor configurations have only been investigated in a few helical devices and the theoretical and experimental efforts mainly concentrated on the suitability of divertor magnetic field structures. Detailed studies of the divertor plasma properties for the two types of divertor configurations have only recently begun. The presently available data are certainly not yet sufficient to compare the advantages and disadvantages of the two approaches.

The paper is organised as follows. In section 2 the helical and island divertor concepts and their physics background are introduced and different physics operational modes discussed. In chapter 3 the helical and island divertor experiments performed and planned for different devices are being reviewed. The status of the divertor plasma simulation codes, which are used for predictive studies as well as for the interpretation of the divertor experiments, are also discussed in this context. Finally in chapter 4 the present status of the divertor concept developments will be briefly assessed.

## 2.     The divertor concepts in stellarators

### 2.1     General considerations

Depending on the stellarator type, divertors are realised in different ways. In moderate to high-shear heliotrons like Heliotron E and J, CHS and LHD one can make use of intrinsic helical diverting field lines to create a helical divertor. By employing additional field perturbation coils these machines benefit from the additional flexibility to create externally imposed islands, which allow the installation of a so called local island divertor (LID). These coils can also be used to correct for any error fields. In low-shear advanced stellarators like W7-AS and W7-X one makes use of the intrinsic islands. This so called island divertor concept has initially been proposed in the 1970s for tokamaks, as small-

current alternative to the poloidal divertor [Karger 1974, 1977] and it is now nearly 15 years that an open and a closed version of an iota(a)=5/9 island divertor has been proposed for the W7-AS stellarator [Karger 1987, Kisslinger]. This concept, though never implemented in tokamaks, evolved to the main route followed in stellarators. Since the field perturbations associated with the islands are very small $\Delta B_r/B_{tor} \sim 10^{-3}$-$10^{-4}$, additional resonant perturbations of the same magnitude created by control coils are sufficient to modify the island geometry, thereby giving control over key parameters for the creation of an effective divertor plasma, like island size, connection length and x-point height above the target.

## 2.2 The helical divertor

The structure of a helical divertor can best be illustrated by Poincaré plots in the poloidal ($\phi$=18°) and the helical plane ($\phi$=0°), (Fig. 2.1) [Ohyabu 1994]. The structure in the
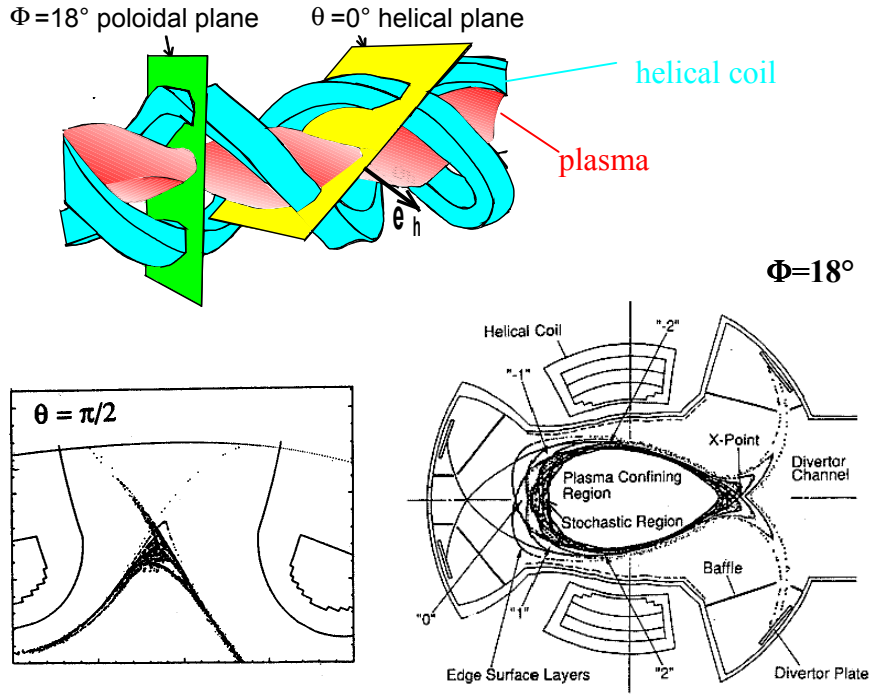


**Figure 2.1:** Schematic view of the LHD helical divertor in the poloidal (Φ=18°) and the helical (θ=90°) plane. [Ohyabu 1994]

poloidal plane is not easy to understand since the divertor regions are helically twisted like the helical coils. In the helical plane the structure near the X-point looks more familiar, since it resembles the one known from tokamaks. However, even though matters are usually discussed in either of these planes, one needs to keep in mind, that the divertor geometry exhibits a strong poloidal variation.

The helical divertor makes use of the inherent magnetic field configuration. The edge magnetic field structure in the poloidal plane is depicted in an exaggerated form (not to scale) in figure 2.2 [Ohyabu 2001]. Just outside the LCMS several island layers with toroidal mode number m=10 are embedded. With increasing radius, the poloidal mode number of the island layers decrease, while the size of the islands increases until the layers begin to overlap, resulting in a stochastic field region.

The stochastic region is followed by a region with multiple thin curved layers, the so called 'edge surface layer region', which is itself bounded by an elliptically shaped boundary, which is often called the separatrix boundary. The size of the 'edge surface layer region' can be optimised with respect to plasma volume, MHD stability and baffling of the divertor chamber, by moving the plasma radially through changing the vertical field (fig. 2.3). Field lines from the stochastic region enter these surface layers and after many toroidal
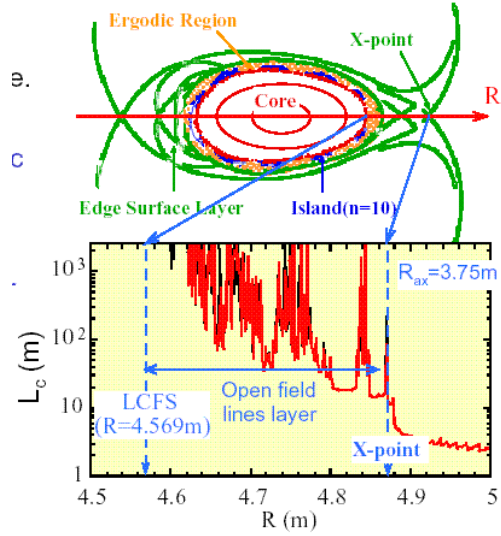


**Figure 2.2:** Schematic Poincaré plot of the edge magnetic structure and the corresponding connection lengths $L_c$ [Ohyabu 2001].
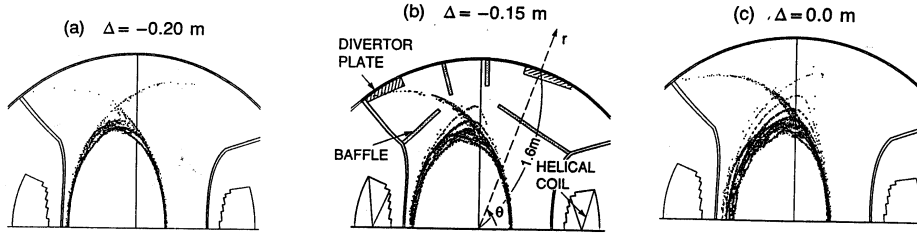


**Figure 2.3:** Effect of a plasma axis shift ($\Delta$) relative to R=3.9 m for LHD on the edge surface layer (at the poloidal plane $\theta$=0°)[Ohyabu 1994].

circulations reach the 'X-point' of the 'separatrix' and then hit the divertor plate. The connection lengths of these field lines are typically of the order of several hundred meters. The regions without points are not connected to the stochastic region but directly to the divertor target plates and therefore only have short connection lengths. The field lines in these regions move as a group in the forward (backward) toroidal direction from 0 => 1(-1) => 2(-2) => ... until they finally reach the divertor plate (see fig. 2.1). The field lines outside the 'separatrix', i.e. also the field lines between the X-point and the divertor, have very short connection lengths of only a few meters. Taking cross-field transport into account by tracing the field lines with a random walk process the wetted areas on the targets were roughly estimated. For a 20 MW discharge run with an optimum configuration a maximum heat flux of approximately 5 MW/m$^2$ is expected for example in LHD.

The X-point itself rotates nearly with the same pitch as the helical coils. The field line distance between the X-point and the divertor plate is very short, of the order of the plasma minor radius. The X-point is located at a minor radius which is close to the minor radius of

the helical coil $r_c$. The helical coils generate a strong axisymmetric toroidal field only inside the region $r < r_c$, while for $r > r_c$ , i.e. beyond the X-point, the toroidal field rapidly decreases. The increase in the local rotational transform is therefore caused by the decrease of the toroidal field $B_\phi$ with increasing r. One should bear in mind here that this cause is quite contrary to the situation in classical stellarator configurations, where it is due to an increase in the poloidal field $B_\theta$. In these configurations $B_\theta$ increases with r since one is getting closer to the helical coils with counter running currents [Ohyabu 1994]. In classical stellarators toroidal coils located outside the helical ones are needed to generate a strong axisymmetric field, since the helical coils cannot provide this because of the alternating direction of the helical coil currents.

On the way to a fully closed helical divertor it is being considered to first use a simpler open divertor with baffles to minimise recycling [Ohyabu 1998, Ohyabu 1999]. A suitable candidate for a divertor upgrade suggested for LHD is the configuration depicted in figure
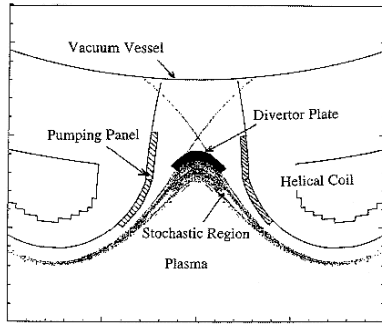


**Figure 2.4:** Candidate for LHD open divertor upgrade [Ohyabu 1999].
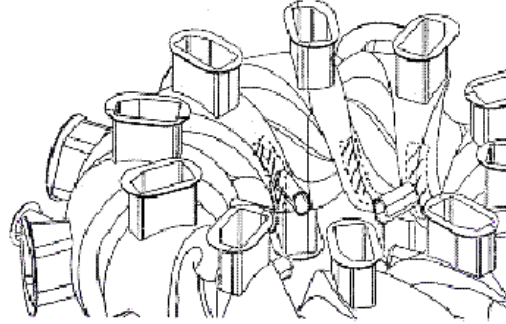
**Figure 2.5:** Locations of the possible upgrade open divertor segments for LHD [Ohyabu 2001].

2.4, which could be installed at the inboard side of the vessel (fig. 2.5). A design study for LHD shows that such a system could withstand 20 MW of heating power and would cost an order of magnitude less than a full helical divertor. 10 units with a helical extension of 2 m and a width of 0.3 m could handle a steady state input power of 10 MWm$^{-2}$. For the simultaneous achievement of H-mode and radiative cooling (SHC operation, see chapter 2.4.1.1), localisation of the recycling in the open region is an important requirement. The concept is believed to be realisable with this configuration because the width of the open plasma region in front of the divertor plate is at least as wide as 10 cm and because the plasma density at the LCMS is expected to be $\sim 2 \ 10^{19} \ m^{-3}$.

## 2.3    The island divertor

The basic idea of the island divertor is to utilise the islands for exhaust. The divertor islands originate from small radial field perturbations $b_{mn}=B^r_{mn}/B_{tor}$. At the radial location where the rotational transform $\iota =M_{per}$ m/n ($M_{per}$ = number of toroidal field periods) has a rational value, a sideband Fourier harmonic $B^r_{mn}$ of the radial $B^r$ spectrum, which is resonant to that rational $\iota$, tears the nested flux surfaces so far apart that magnetic islands are formed. This process can roughly be described as follows: The radial component of a perturbing field $B_{mn}$, $B_r=-B_{mn} \sin(n\theta)$, tears a magnetic field line away from a resonant surface. Its radial deviation from the resonant surface is $d\Delta r/d\Phi \approx -R\ b_{mn}$



**Figure 2.6:** Iota-profile dependence of island formation [Wobig 1987, Brakel 2000]

$\sin(n\theta)$. With $d\theta = \Delta r\ \iota'\ d\Phi$ ($\iota'=d\iota/dr=$ magn. shear), integration then yields $\Delta r^2=2\ R\ b_{mn}/n\ \iota'\ [1+\cos(n\theta)]$, by making use of $\Delta r=0$ at $n\theta=\pm\pi$. This eq. describes the poloidal modulation of the radial distance of a magnetic field line from an undisturbed resonant surface, leading to the formation of magnetic islands with a radial width of $r_i = \Delta r(\theta=0)$ $=2(Rb_{mn}/n\iota')^{1/2}$. The poloidal width of an island scales as $\delta_{pol} \sim$ a/n, (a: minor radius). The harmonics reflect the inherent non-axisymmetry of the configurations and the properties of the modular coils. The largest islands appear at the edge at the lowest order resonances, i.e. for the lowest m (often m=1). As figure 2.6 shows [Wobig 1987, Brakel 2000], at low shear $\iota'$ the islands can become large, but also can be avoided altogether by an appropriate choice of $\iota$, while at large shear the



**Figure 2.7:** 'Natural island chain of the i=5/9 resonance in the triangular and elliptical plains of W7-AS [Sardei 1997]

islands cannot be excluded and the islands become small and increase in number. In W7-AS and W7-X the rotational transform can for example be varied in the range from 0.3-0.7 and 0.83-1.25 respectively by adjusting the ratio of modular to toroidal field coils. In W7-AS for example only the low-order m=1, n=8-10 islands have a divertor relevant size, and the best compromise in terms of island and core plasma size, is $M_{per}$=5, m=1 and n=9. Poincaré plots of the chain of 9 'natural' islands resulting from such a $\iota_a$ =5/9 resonance are shown in figure 2.7 [Sardei 1997]. The diversion property of the islands results from the finite shear at the edge. The rotational transform can be separated into two parts, i.e. $\iota = \iota_{5/n} + r_i\ \iota'$. The first term describes only the helical rotation of the islands around the torus at the 5/n resonance, while the second one, which describes the internal poloidal pitch of the field
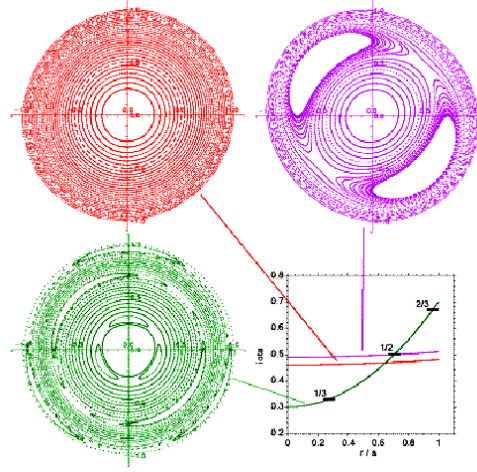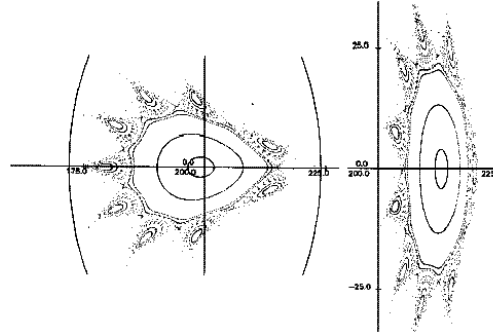
lines around the island centre (O-point), is the important one for the functioning of the island divertor concept. Island size and shear are geometric parameters which largely determine plasma transport inside the islands. Their impact on cross-field transport has already been assessed theoretically as well as experimentally in W7-AS (see chapter 3.5.2).

The $\iota$-profile determines the topology of the islands. One differentiates between topologically *closed* and *open islands*. If in low shear configurations the intrinsic perturbation field is sufficiently weak, as e.g. in the W7-X standard case ($\iota_a$ =1), the island region can be topologically 'closed', i.e. true flux surfaces exist and can be used for mapping experimental data and for defining a 3D modelling grid. A small reduction of $\iota_a$ relative to this case, caused by an increase of the intrinsic perturbation field as the plasma gets closer to the coils, e.g. by a radial outward shift of the plasma by an imposed $B_z$-field, or by raising the field of special island divertor control coils [McCormick 1999], or by plasma pressure effects [Strumberger 1999], is sufficient to cause an outward shift of the island chain and a break-up and ergodisation of the island flux surfaces, beginning at the separatrix and gradually extending towards the O-point (*'open' island case*). With decreasing $\iota_a$ one finally gets a chain of strongly diverted island fragments. These are regularly distributed according to the poloidal mode number of the island resonance. Fortunately the degree of ergodisation in the low shear configurations of W7-AS and W7-X is still sufficiently low as to not destroy the basic field structure of the dominant $\iota_a = 5/n$ edge resonance, so that the regular field structures can still be represented by nested 'open magnetic surfaces', spanned by field lines for which generalised flux co-ordinates can be obtained [Sardei 1994]. While until recently it was only because of these remaining regularities possible to still create a mapping framework for all 'open' edge configurations of W7-AS in the $\iota$ range relevant for divertor operation, now even open islands and ergodic regions can be treated properly. A newly developed 'reversible field-line mapping (RFLM) technique has recently been implemented in the EMC3/EIRENE code which removes this limitation [Feng 2001].

Although with an island divertor (ID) one is aiming at influencing the same parameters as in a tokamak and is trying to do this in a similar fashion, the dominant processes that are used to create similar conditions in front of the divertor target plates are quite different in stellarators. This is largely due to the fact that a number of leading geometrical parameters are significantly different in stellarators:

- field line pitch 0.001-0.005 compared to 0.1 for tokamaks
- connection length for IDs generally larger than for large tokamaks due to low $\iota$ inside island islands (fig. 2.8)
- distance main plasma – target much smaller than in tokamaks leading to a less efficient screening of recycling neutrals
- the larger $L_c$ and the smaller plasma-to-target distance causes that cross-field transport plays a stronger roll in stellarators than in tokamaks
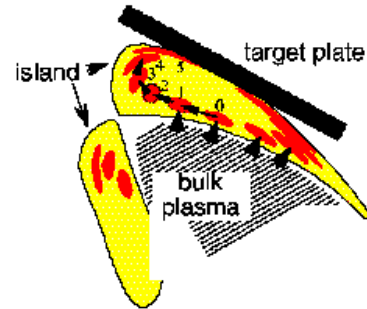- IDs are inherently three-dimensional



**Figure 2.8:** Poloidal movement of a flux tube per toroidal module in W7-X.

The required discontinuous target plates imply a toroidal localisation of recycling neutrals and ionisation sources. The targets are usually placed at the elliptical cross sections where the islands have their largest radial extent and their largest distance from the magnetic axis (fig. 2.9). While for low recycling conditions ionisation takes place inside the LCFS, under high conditions the particles are getting ionised inside the islands, i.e. the recycling fluxes are focussed predominantly into the islands, enhancing the effect by building up even more density

**Figure 2.9:** Magnetic island intersected by a target plate [Sardei 1997]

in there (2.10a,b). The fact that the island SOL is poloidally closed in front of the targets, enables more efficient trapping of the recycling particles than in comparable tokamaks, thereby compensating for the fairly short distances between the targets and the LCFS and ensuring a sufficient de-coupling of the recycling neutrals and target-released impurities from the plasma core. Earlier EMC3/EIRENE calculations performed without taking impurities into account and without parallel momentum losses being fully implemented, already showed [Sardei 1997] that for the W7-AS
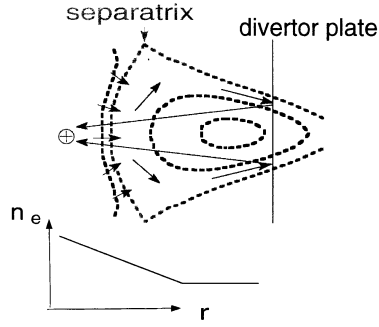
**Figure 2.10a:** Principle of low recycling inside islands intersected by a target plate. [Sardei 1997]
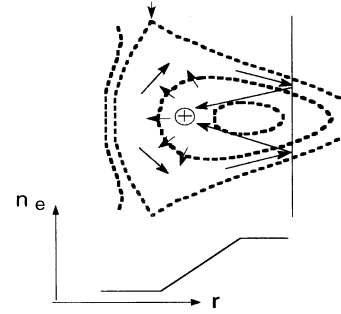
**Figure 2.10b:** Principle of high recycling inside islands intersected by a target plate. [Sardei 1997]

island divertor geometry ionisation inside the islands leads to a strong density rise inside the islands. The maximum efficiency in terms of recycling and diverting property of the islands can be reached when parallel and cross field heat transport are roughly in balance (in tokamaks parallel heat conduction always strongly dominates transport from up- to downstream, while cross-field transport only results in a finite radial width of the SOL in these machines). This condition is fulfilled when the temperature gradient scale length $\lambda_T$ becomes comparable to the average radial extension of the island region intersected by the target plates [Sardei 1997]: $\lambda_T / \delta = 7/4 \; L_c \; (\alpha \; \chi_\perp \; n_u / \kappa_0 \; T_u^{5/2})^{1/2} \; / \; \delta \approx 1$ with $\alpha \equiv (1-0.5 \; L_x/L_c) \; L_x/L_c$ and $L_x/L_c$ being the fraction of the connection length facing the core plasma. Here it is assumed, that the influx into the island only takes place at the interface between island and main separatrix, while the influx from the sides of the island, which might as well play a significant role, depending on the particular conditions, has been neglected here. Typical values for W7-AS are $\lambda_T / \delta \approx 0.45$.

A further useful expression telling when parallel dominates over the cross-field poloidal heat conduction is [Feng 1999]: $T_e > (\chi \; n_e/\theta^2 \; \kappa_e)^{(5/2)}$, with $\theta$: field line pitch and $\chi = \chi_e + \chi_i$. For $\chi_\perp = 2m^2/s$ and $n_e = 5 \; 10^{19} \; m^{-3}$ one gets for a tokamak ($\theta=0.1$): $T_e > 1$ eV while for the

8

W7-AS divertor ($\theta$=0.001) one gets $T_e > 36$ eV. Therefore in tokamaks parallel heat conduction is usually dominate throughout the SOL, while in the island divertor the situation is more complex. 'Upstream' usually parallel heat conduction governs the energy transport since the temperature there is usually $> 36$ eV, while further downstream towards the target with falling temperature parallel heat flux is gradually exchanged for perpendicular one. This effect could reduce the impurity influx since the cross-field poloidal energy transport can smooth out the strong parallel temperature gradient close to the targets and can thereby reduce the thermal force acting on the impurities, which tends to drive the impurities away from the targets up to the X-point. For cold islands cross-field heat conduction could become dominating throughout the island SOL, thereby causing $T_{eu}$ to decrease with increasing $n_{eu}$ at high densities (Two-point model).

An important effect not known from tokamak divertors is the loss of parallel momentum through strong anomalous shear viscosity between the counter streaming particles in adjacent island fans, due to their relatively small radial scale length. (fig. 2.11) The momentum loss due to the counter streaming particles can be roughly estimated by: $M_{loss} = p_u - 2\, p_d = \nabla_\perp (-D\, \nabla_\perp\, m\Gamma_\parallel)\, dl_\parallel$ ; $\Gamma_\parallel$: parallel particle flux, $dl_\parallel$ integration along field line. By using a simplified 2-D geometry with a continuous target this equation can be solved analytically, resulting for W7-AS in a ratio of $M_{loss} / p_d = 1.3$, i.e. the small island size and long connection length leads to significant momentum loss by cross-field diffusion [Feng 1999].



**Figure 2.11:** Friction between two counter streaming fans causes momentum losses by radial shear viscosity. [Sardei 2001]

Another effect, not known from tokamaks, which also leads to momentum losses, arises from the three-dimensionality of island divertors. The discontinuous target plates cause, in addition to the standard parallel temperature gradients associated with the heat conduction to the targets, a local strong periodic interaction of the out-flowing plasma with recycling neutrals and target released impurities, which no longer smoothes out for downstream temperatures $T_d<10$eV. Figure 2.12 illustrates the process. A parallel flux tube of long connection length (main flow) terminates on the left target. Due to the long distance between the two plates (9/2 field periods in W7-AS) and the small field line pitch, a large number of particles can diffuse poloidally into the shadowed region between the targets and thus carry momentum away from the main flux tube. Part of these particles even flow back to the target on the right and thereby cause friction to the main streaming ions [Feng 1999].

EMC3/EIRENE calculations showed further that neutral compression due to target inclination and baffles should lead to neutral densities in the divertor chamber more than two orders of magnitude higher than outside of it.
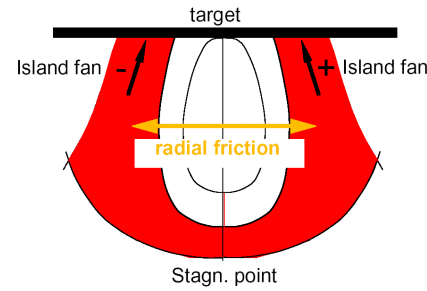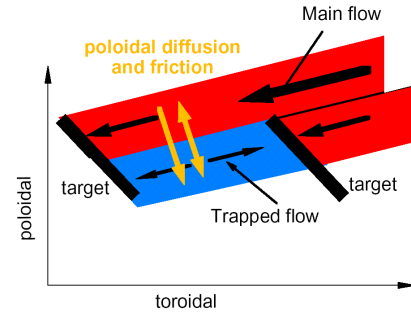


**Figure 2.12:** Poloidal diffusion into shadowed region and friction between main flow and trapped flow cause momentum loss by poloidal diffusion and shear viscosity. [Feng 1999]

Detailed theoretical studies concerning the transition to detachment in an island divertor configuration have been undertaken in the course of the last years, mainly with the aim to predict the behaviour of the W7-AS island divertor recently installed. This has been done on different levels, from simple two-point and 1-D models [Feng 1999, Feng 1999a], giving easy direct physical insight into the processes involved, to 2-D B2/EIRENE [Braams 1986, Reiter 1984, Herre 1997, 1999,Feng 2000] (based on helically averaged island geometry and a continuous divertor plate, sputtered carbon as radiating impurity) and full 3-D EMC3/EIRENE [Feng 1997, Feng 1999a] (Monte Carlo code solving a set of stationary Braginskii fluid equations in 3D space, self-consistently treating plasma, neutrals and impurities taking into account the complex 3-D island structures and discontinuous divertor plates and baffles) calculations providing the most sophisticated prediction of all relevant parameters so far.

Within the framework of the two-point model low and high-recycling regimes can clearly be identified. The model predicts a sharp transition from low- to high recycling accompanied by a steep rise of the downstream density and a strong drop of the downstream temperature (fig. 2.13). The EMC3 code calculations (impurities not included) confirm the general trends of the simple model but show a smoother change of $T_d$ and $n_{ed}$ with $n_{eu}$. They also show the island divertor specific, strong momentum loss at relatively low densities arising from cross-field transport. Moreover the EMC3 calculations reveal a linear drop of $T_u$ with $n_{eu}$ at high densities, indicating that the cross-field heat conduction dominates over the parallel one [Feng 1999b]. With a 1-D radial energy transport model it was possible to reproduce the sharp transition and jump of the radiation zone at the transition to detachment. The model showed, for $P_{SOL}$=1 MW, $n_{eu}$=8 $10^{19}$ m$^{-3}$, $\chi$= 3m$^2$s$^{-1}$, that at a carbon concentration between 1.3 and 1.4% the radiated power fraction jumps from ~30 to ~100%. Fig. 2.14 shows the resulting location of the radiation zones above the target for both the attached and detached state together with the temperature profile. From this model a simple condition for stable detachment can be derived:

$$\text{const.} \, (C\chi \, n^3)_{x\text{-target}}^{1/2} > q_u > \text{const.} \, (C\chi \, n^3)_{x\text{-u}}^{1/2}$$

with    const. = $({}_0\!\int^\infty L(T) \, dT)^{1/2}$,
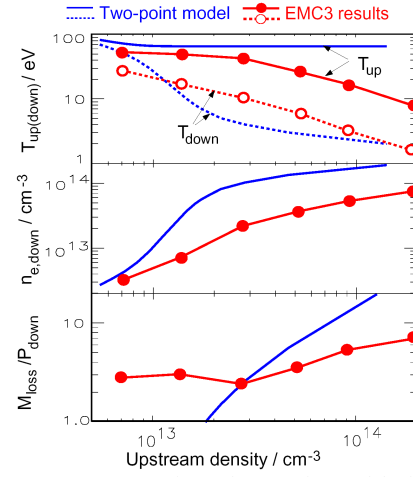        $L(T)$: cooling rate function



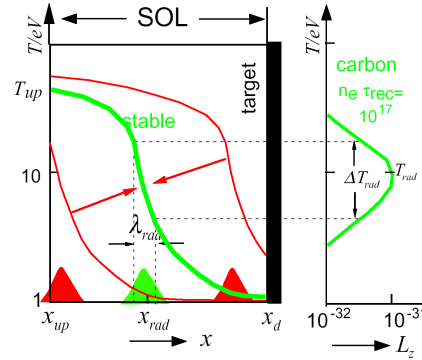**Fig. 2.13:** Comparison of two-point model with EMC3 calculations. [Feng 1999b]



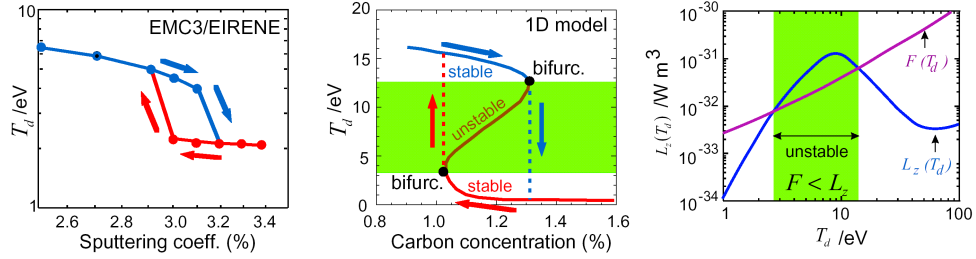**Figure 2.14:** Location and width of the detached radiation layer. [Sardei 2001]

10

**Figure 2.15:** Two branch transition (hysteresis loop) between attached and detached state. [Feng 2001a]

From this follows that detachment is stable within the SOL if the radiation capability is higher than the input power at the target and lower at the upstream SOL position [Feng 2001, 2001a,b]. Detailed modelling with the EMC3/EIRENE code (parameters as above, but D=0.5 $m^2s^{-1}$, $\chi_e$= $\chi_i$= 3D) showed that the transition into and out of detachment occurs at different total carbon sputtering coefficients giving rise to a hysteresis loop (fig. 2.15) [Feng 2001a]. This effect is related to the form of the cooling rate function L(T). The simulations show further, that the radiation zone is thin (~1cm) (fig. 2.14), compared to the island size (~5cm), and jumps from the target to the X-point at detachment [Sardei 2001]. For higher upstream densities the transition finally becomes smooth (fig. 2.16).
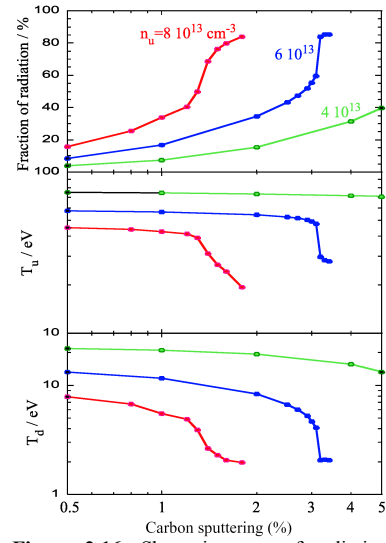


**Figure 2.16:** Sharp increase of radiation and drop of T at detachment transition.. [Feng 2001, 2001a]

11

## 2.4 The Local Island Divertor (LID)

The LID is a closed divertor utilising the island geometry [Komori 1994]. In order to establish the required magnetic configuration in a Heliotron device an additional set o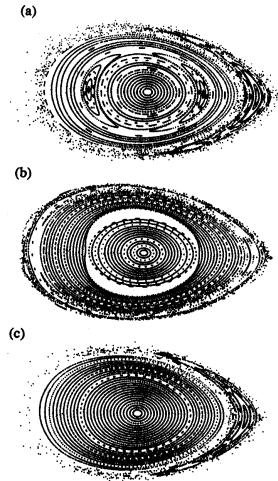f control coils is required. Fig. 2.17 shows the coil set installed in LHD above and below the cryostat. By proper arrangement of the currents in the different control coils, a magnetic configuration consisting of a clean $m/n=1/1$ island at the $\iota/2\pi = 1$ surface with an almost eliminated $m/n=2/1$ island at the $\iota/2\pi = 0.5$ surface can be established (fig. 2.18). Fig. 2.19 shows the $m/n=1/1$ island geometry as it is utilised for a LID. The divertor head is inserted into the island such that the leading edges are inside the island and thereby get not exposed to the exhaust (fig. 2.19, 2.20). The heat and particle flux leaving the confined plasma crosses the island separatrix by perpendicular diffusion and then flows along the field lines through a narrow gap between the exhaust duct and the LID head towards the target plates on the back side of the head. Because one thereby forces recycling to take place in a fairly closed chamber one expects to achieve a pumping efficiency of up to 30 % by attaching a cryopump to the exhaust duct. In contrast to the helical divertor, in which the transition from the LCMS to the open region takes place in a very fuzzy, gradual way over more than ~50 mm, it is a characteristic feature of the LID that the transition happens radially very sharply within 2 mm. This feature is believed to be important for generating an H-mode thermal barrier, which typically has a width of 10-20 mm, just inside the LCMS. With this type of a closed divertor it is hoped to achieve a considerable improvement in $\tau_E$ for $\iota/2\pi = 1$.
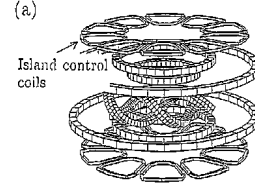


**Figure 2.18:** Magnetic surfaces created by adding resonant perturbation fields to the standard LHD magnetic configuration. The perturbation fields are generated by (a) two pairs of adjacent island control coils above and below the torus, (b) another pair of coils at right angle to those of (a), and (c) these three pairs of coils with a proper coil current distribution. [Komori 1994]



**Figure 2.17:** A set of 20 LID coils is used in LHD. [Komori 1994]
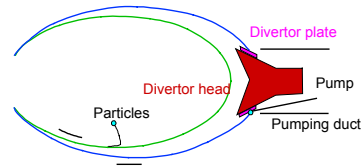


**Figure 2.19:** LID configuration and particle flow to divertor plates. [ Komori 1998]
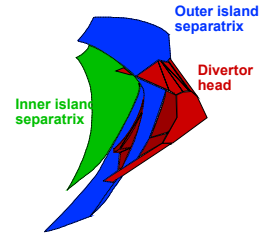


**Figure 2.20:** Schematic view of the LID explaining the relation between divertor head and island separatrix. [ Komori 1998]

### 2.4.1 LID configuration based divertor operational modes

Two further operational modes based on LID field configurations are expected to give access to new operating regimes: low temperature, radiative operation and high temperature divertor plasma operation [Ohyabu 1994a, 1995, 1998].

#### 2.4.1.1 Low temperature radiative divertor plasma operation

The possibility to form an m/n=1/1 island surrounded by an open ergodic boundary (fig. 2.21) opens the unique opportunity to combine an H-mode compatible low density edge region with a radiative cooling layer with a wide heat flux distribution. (SHC operation: Simultaneous achievement of H-mode and radiative Cooling)

When a low m single island layer is located in the inner ergodic region *(LID operation without inserting the head)* (fig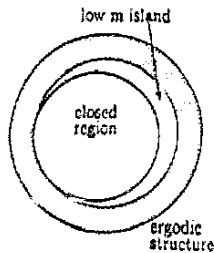. 2.22), then temperature and density are constant along the island and thus the density at the LCMS can be kept low. The low m island serves to sharply separate the closed surface region from the high density, radiative boundary with $\nabla_{\parallel}p=0$. This configuration is similar to that of the conventional poloidal tokamak divertor, but with the significant difference of a large radiative cooling volume (~10% of $V_p$). The connection length between a point just outside the LCMS and the divertor plate is ~200 m, which is similar to a tokamak with long divertor channels (fig. 2.23). In this approach the magnetic configuration is the same as that for the LID, however without the LID head inserted into the island and with pumping not being essential.
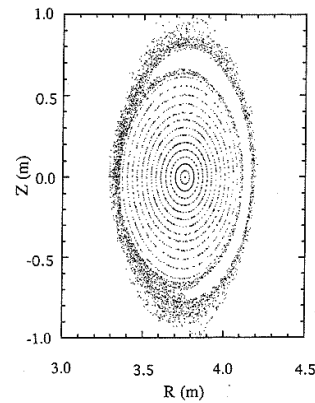


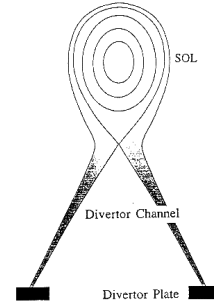**Figure 2.21:** m/n=1/1 island configuration. [Ohyabu 1998]



**Figure 2.22:** Separation of the closed surface region and the high density, radiative boundary. [Ohyabu 1995]



**Figure 2.23:** Similar, large divertor volume, poloidal divertor (tokamak). [Ohyabu 1998]

#### 2.4.1.2 High temperature divertor plasma operation (HT operation) [Ohyabu 1994a, 1995, 1998]

It is believed that high divertor temperature low recycling operation is a prerequisite to enhanced energy confinement in tokamaks and helical devices [Ohyabu 1992, Ohyabu 1993]. From power balance considerations it has been estimated, that in an NBI heated plasma divertor temperatures of 4-5 keV should be achievable in LHD by efficient pumping in the divertor chamber. Efficient hydrogen pumping could possibly already be achieved in LHD with an open, but baffled, helical divertor with additional carbon sheet [Sagara 1995]

or membrane [Livshitz 1990] pumping panels (see fig. 2.4), while for reactor applications a new divertor magnetic field geometry has been suggested, which guides the outward flowing plasma to a very remote area [Takase 1994]. To maintain peaked density profiles a combination of deep fuelling by NBI heating or pellet injection and efficient pumping could be employed. Under these conditions particle confinement considerably influences energy confinement. This is particularly important in LHD since it can counteract the effect of high ripple induced electron heat losses which tend to lower the edge temperature gradient. The effective particle diffusion coefficient is not particularly high though, since the ions are well confined by the E x B drift. An advantage is however that the radial electric field in this regime is positive, so that the neoclassical outward impurity pinch is hoped to prevent impurity accumulation. In tokamaks impurity accumulation could be a major obstacle for HT operation since the neoclassical impurity pinch is directed inwardly in these machines.

### 3. Helical and Island Divertor Experiments

Within about the last 15 years considerable progress has already been made in the understanding of what role different divertor types could possibly play in present day and future helical devices. Our understanding of the functioning of the different divertor concepts is not only based on a large theoretical effort but also on a considerable number of experimental tests performed on different helical devices. In the following it will be attempted to summarise the main insights gained from experiments performed on a number of different machines which had run dedicated divertor experiments.

### 3.1 Heliotron E

Heliotron E was a planar axis heliotron with a l=2/m=19 helical coil (m: helical pitch number). The magnetic field in this machine was controlled by additional toroidal and vertical field coils. The investigation of a helical 'whisker-like' divertor configuration, as described in section 2.2, was one of the principle purposes of this machine [Matsuura 1992, Obiki 1988, Motojima 1984]. Fig. 3.1 shows a plot of such a configuration produced in

Heliotron E. As the figure shows the stochastic magnetic field lines outside the LCFS form flux bundles, which in this machine simply intersected the chamber wall. The intersection points concentrate in a very narrow region (the 'divertor trace') in the $\theta-\phi$ (pol.-tor.) plane. As expected, the edge plasma has been found to flow along these distinct flux bundles to the wall. Since the flux bundles terminate at a metal surface (the vacuum chamber wall), ambipolarity in the plasma flow is not required in a local area and the edge transport might be affected by the electric field due to this non-ambipolar flow in the edge region [Mizuuchi 1991, Chechkin 2000, Zushi 1996, Chechkin 1997, Boykov 1998]. It is assumed that not

**Figure 3.1:** Poincaré plot of the divertor region The stochastic region with $L_c > 5m$ is indicated. [Motojima 1984]

every field line in the stochastic region has a characteristic which works as a divertor, but more than 90 % of the charged particles are expected to flow along the field lines of the stochastic region to the wall [Motojima 1984]. Experiments have shown, that there are divertor traces on the surface of the vacuum chamber. The charged-particle flux is
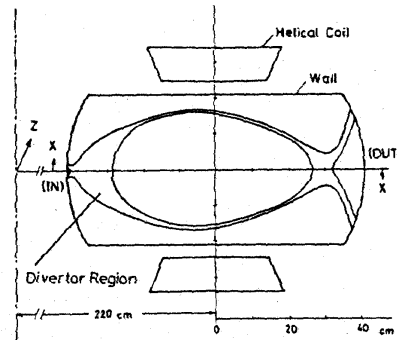
concentrated on these traces and the plasma-wall interaction occurs there. Langmuir probe and calorimeter (fig. 3.2) measurements have been performed across the divertor traces near the wall. The half-widths of the ion saturation current and of the time averaged heat flux, were about 2 cm. These widths were consistent with what one expected from field structure calculations taking particle diffusion inside the region r < 31.5 cm into account. With this width the total divertor trace area was estimated to be ~2.7 m$^2$ or ~8 % of the total inside surface area of the vacuum chamber. The experiments in Heliotron E showed that the density and heat flux distribution was sharply localised in a narrow region where the field lines had long connection lengths $L_c$. It was found that the shape and the position of the
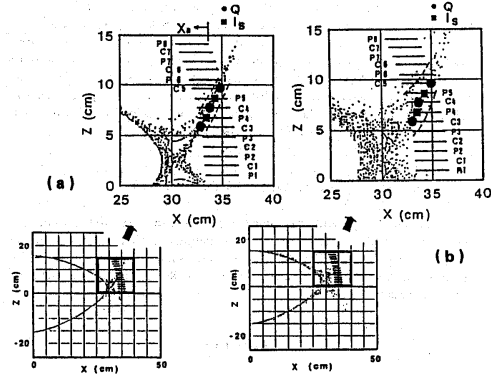


**Figure 3.2:** Comparison of measured peak and half maximum (---) ion saturation current (■) and heat flux (●) for two different ratios of vertical ($B_v$) to toroidal ($B_o$) field strengths (a) ß = -0.1873 and (b) ß=-0.173. The lower figures show the Poincaré plots. The horizontal lines mark the measurement range of the moveable Langmuir probes and calorimeters. [Obiki 1988]

distributions were fairly insensitive to changes in density, input power or vertical field strength. The estimated total heat flux in divertor field region was found to be roughly balanced with $P_{in}$ - $P_{bolo}$ [Obiki 1988].

An up/down asymmetry in the peak particle and heat flux has been observed which might be caused by an ion grad B drift [Matsuura 1992, Mizuuchi 1991]. The possibility that the grad B drift plays an important part in the particle flow is supported by floating potential measurements, which showed non-uniformities in poloidal and toroidal directions, which suggest that the ambipolarity of the plasma is broken in a local area. It has been observed that the polarity of the floating potential of many metal calorimeter plates was consistent with the direction of the grad B drift and was reversed by the change of the helical field direction.

A shift of the magnetic axis has a strong effect on plasma confinement, not only in Heliotron-E but also in other heliotron-type devices such as Heliotron-DR, CHS, ATF and LHD. An auxiliary vertical field (causing a radial shift) however was found to have little effect on the edge structure. For the design of a helical divertor, this is a good property since high ß operation is naturally accompanied by a shift of the magnetic axis [Matsuura 1992].

When the confinement volume is changed with the help of an additional toroidal field, there is a shift of the edge density and temperature profile. The toroidal field has a strong effect on the position of the divertor trace. It moves towards the midplane with increasing field and departs from it with decreasing field [Matsuura 1992].

Error field coils were used to produce artificially destroyed magnetic field lines with m=1/n=1. Field line calculations show that a large island appears at the rational surface (iota=1) and the magnetic surfaces around this island become ergodic. The central plasma parameters are not affected, but the edge density reduces by ~ factor 10. The error field was not so strong as to destroy the divertor trace structure [Matsuura 1992, Obiki 1990].

Experiments with stainless steel baffle plates installed in one-fifths section of the torus to investigate the effect of retaining the recycling neutrals have been performed (fig. 3.3). To avoid melting, the throat in the baffle plates had to be somewhat wider than the width of the divertor layer, so that in effect a leaky divertor chamber was created. The divertor plasma parameters ($n_{ed}$, $T_{ed}$) showed little or no difference with or without baffles, only the

neutral densities in the baffled and non-baffled sections seemed to be somewhat different. The reasons why the baffled section had so little effect were believed to be the short field line length inside the 'divertor chamber' $L_b$, i.e. from divertor throat to the divertor plate (the wall) and the low ionisation rate in the thin divertor plasma. The short connection length $L_b$ makes it difficult to sustain a gradient in the plasma density and temperature along the field line and the low ionisation rate results from the separatrix not being baffled all around the torus [Obiki 1990].



**Figure 3.3:** Poincaré plot with baffle plates installed. [Obiki 1990]

The edge plasma behaviour has been investigated in different in ECR and NBI heated plasmas. High power ECH had been found to lead to a degradation of particle confinement, a decrease of the central density ('density clamping') and an increase in the edge density. The heat losses to the inboard divertor with increasing NBI power were observed to increase rapidly, most likely due, to theoretically predicted, enhanced direct losses of deeply trapped particles in that region. The total heat loss to the divertor region (estimated under the assumption of a constant heat loss in toroidal direction, by summing over the three peak heat flux densities multiplied by their half widths in poloidal direction) is almost equal to the input power and the fraction deposited in the divertor increased with plasma density, which is preferential for any divertor design. The divertor density was approximately proportional to the line averaged density of the core plasma. According to a simple particle balance model, the divertor plasma density is proportional to the line averaged density of the core plasma and inversely proportional to the connection length to the wall. Since the connection length of the magnetic field in heliotrons is short, this model can explain the results [Matsuura 1992].
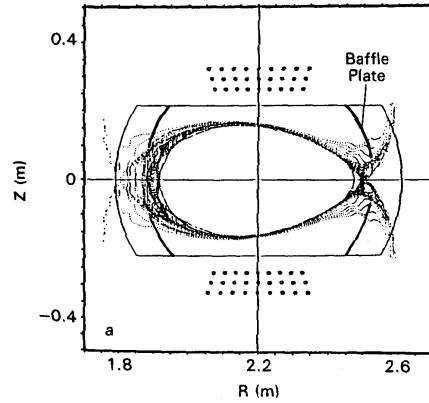
### 3.2 Heliotron J

Heliotron J, which went into operation in July 2000, is a l=1/M=4 helical-axis heliotron device [Obiki 1999, 2000]. It is planned to install a divertor for phase II starting in 2003. This requires the installation of a modified coils assembly.

One of the main design goals of Heliotron J is the comparison of the advantages and disadvantages of helical/island divertor concepts and the development of advanced and possibly innovative divertor structures for helical axis heliotron devices [Mizuuchi 1999]. Owing to the flexibility of field configuration control in Heliotron-J, helical (similar to the conventional 'whisker-structure') and island divertor (island-chain structure) configurations can be realised in one and the same device. When $\iota/2\pi$ is far from any low mode resonance condition the topology similar to the conventional helical divertor is found, while when $\iota/2\pi$ is close to a low rational number, a clear island chain is observed outside the LCFS.

#### 3.2.1 Helical configuration

A helical divertor configuration, which is similar to the conventional heliotron configuration with ergodic edge field lines ('whisker-structure'), is from the viewpoint of plasma confinement the prime candidate for "the standard divertor configuration". The field structure of this configuration becomes rather simple since the field lines cross the wall before the so-called "fold and stretch" effect becomes noticeable (Fig. 3.4 and Fig. 3.5). The connection length of the divertor field lines is much shorter than for the island divertor cases. The connection length of a field line starting 5 mm outside the LCFS is
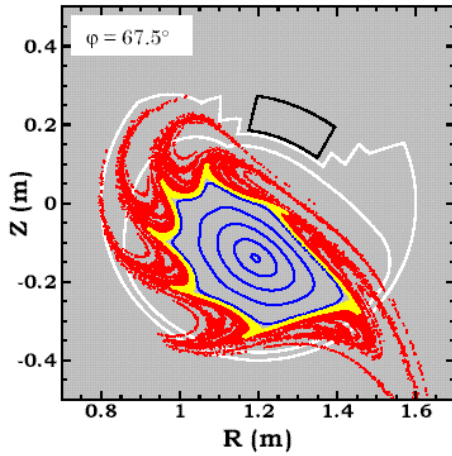


**Figure 3.4:** Poincaré plot of helical divertor configuration (yellow & red dots: open field lines; yellow dots made by field lines started 1 & 5 mm outside LCFS). [Mizuuchi 1999]
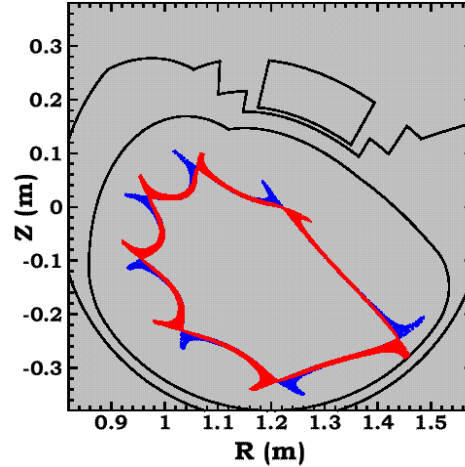
**Figure 3.5:** Poincaré plot of helical divertor configuration, cutting field lines at the wall. The colours differentiate between co- and counter field line tracing. [Mizuuchi 1999]

~40m, while it would be ~300 m or more for example for an m/n=7/4 island divertor configuration. On the low field side only one or the other of the two divertor legs, the clockwise or the counter-clockwise one, attaches to the wall depending on the toroidal location. In contrast to the helical divertor in Heliotron-E, where the divertor trace runs continuously along the torus helically, the divertor footprints are not only localised in poloidal but also in toroidal direction (fig. 3.6). The divertor footprints appear mainly at the low-field side but some interaction also appears at the high field side. The ratio of divertor footprints on the low and high field sides can be controlled by setting and shaping the target plates appropriately. The field line pitch $(B_R^2 + B_z^2) / B_\varphi^2$ is ~0.4-0.45 for the low field line legs and ~0.6 for the high field side ones.
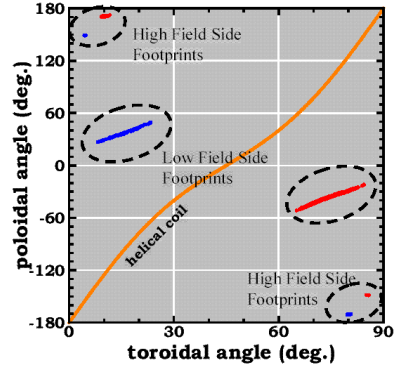


**Figure 3.6:** Footprint locations on the wall surface. Colours see fig. 3.5 [Mizuuchi 1999]

### 3.2.2    Island divertor

Two different modes of island divertor structures with m/n=7/4 ($\iota/2\pi \approx 0.57$) and with m/n=8/4 ($\iota/2\pi \approx 0.5$) can be produced.

### 3.2.2.1        Configuration with m/n=7/4 island

In this configuration the centre of the islands (O-points) is far from the confinement region (fig. 3.7). Although the basic mode of this island is m/n=7/4, a detailed survey of the field topology shows that some other islands exist around an m/n=7/4 island. As in the helical case two footprints exist at the wall on the low field side, one originating from the co- and one from the counter field line direction. The footprints can be moved to the high field side by positioning a target plate somewhere appropriately above the wall on the high field side (fig. 3.8). The connection lengths in the
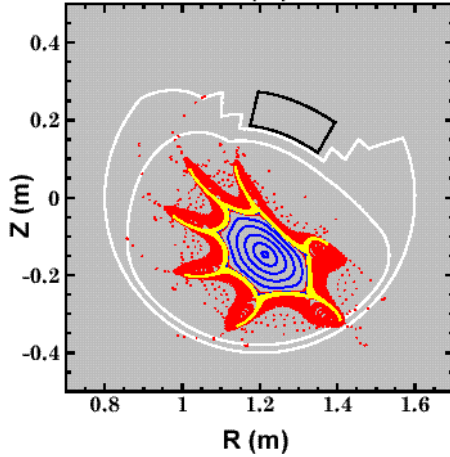


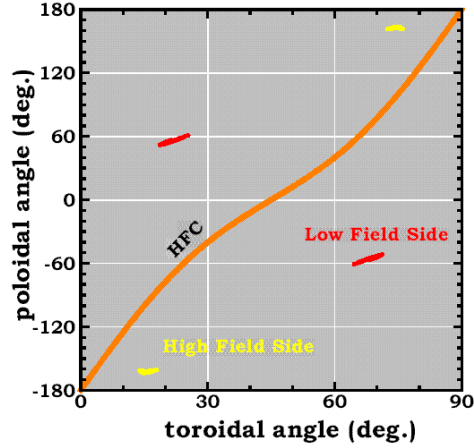**Figure 3.7:** Poincaré plot of m/n=7/4 island divertor configuration. [Mizuuchi 1999]



**Figure 3.8:** Footprint locations on the wall surface for m/n=7/4 island divertor configuration. [Mizuuchi 1999]

m/n=7/4 island case are very much longer than for the helical case. Moreover the divertor legs are fairly long, similar to a high X-point case in tokamaks. The fact that the field strength changes along a field line as a function of distance from the target plate (fig. 3.9) can be used to investigate $\nabla$B-effects along the field line on edge particle and heat transport.



**Figure 3.9:** Change of the field strength along the field line. [Mizuuchi 1999]

### 3.2.2.2    Configuration with m/n=8/4 island

Characteristic for this configuration is that the centre of the island (O-points) is close to the confinement region. The islands of this configuration are actually located inside the LCFS, but by placing the target plates at the island position this configuration can also be used as an island divertor. In fig. 3.10 an example of an Poincaré plot with a target placed 26 cm from the wall in each period is shown.
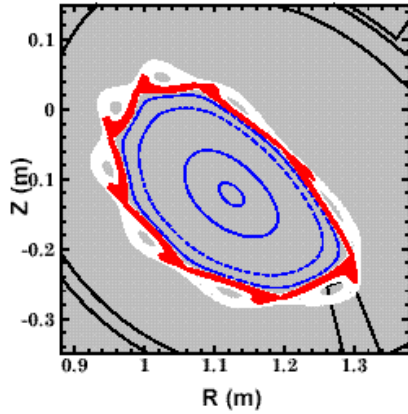


**Figure 3.10:** Poincaré plot of m/n=8/4 island divertor configuration with an artificially introduced localised target block. (white: field line structure without target block) [Mizuuchi 1999]
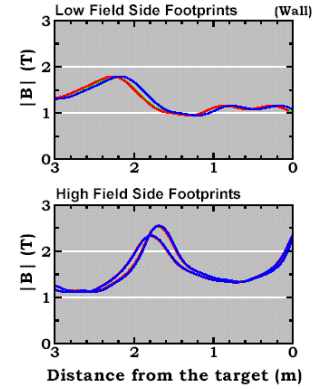
The influence of particle diffusion perpendicular to the magnetic field lines has been simulated by a random walk process in the field lines, corresponding to an effective perpendicular diffusion coefficient of D $\approx$ 1 m$^2$/s. Fig. 3.11 shows all three configurations with diffusion taken into account. The calculations show, that in the case of the helical divertor diffusion does not affect the width of the divertor legs, due to its short connection lengths, while it does expand the width of the legs of m/n=7/4 island divertor configurations. For the m/n=8/4 configurations diffusion is only dominant if only one target is used, its effect however becomes much less important if targets are placed in every field pitch. While in Heliotron-E the divertor traces were continuously running helically around the torus, all 3 divertor structures of Heliotron J are toroidally discontinuous local divertor structures. Only future investigations will tell which of the two concepts is more advantageous.
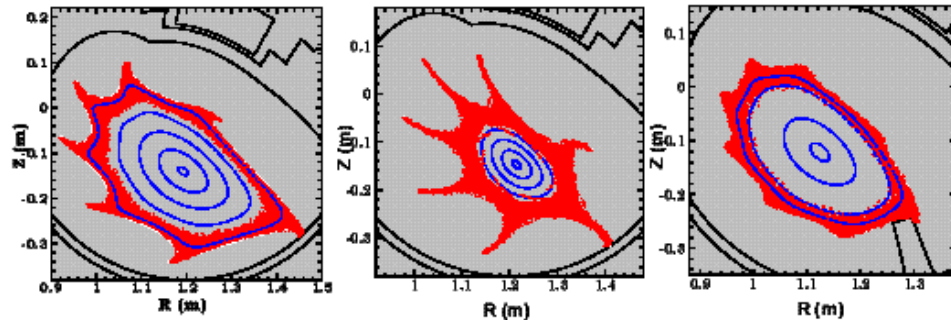


**Figure 3.11:** Effect of particle diffusion simulated by field line diffusion for (a) a helical divertor , (b) a m/n=7/4 island and (c) a m/n=8/4 island divertor configuration. [Mizuuchi 1999]

Another m/n=8/4 island configuration has recently been constructed [Mizuuchi 2001], which constitutes a fair compromise between core plasma and island size (fig. 3.12). In this configuration a target is placed at $r_{target}$ = 0.33 m, i.e. ~5 cm from the chamber wall. This results in a clearance of 2-3 cm on the HFC side. In this configuration the divertor field crosses the target at four discrete regions per field period (fig. 3.13). The total wetted area on the target plate around the torus has been estimated from these calculations to 600 cm2, which corresponds to about 1% of the total surface area of the LCFS. Fig. 3.14 shows the distribution of the field line connection lengths at the footprint location A1 of fig. 3.13.
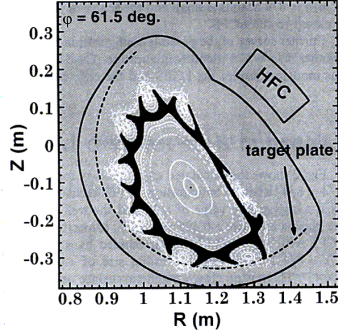


**Figure 3.12:** Poincaré plot of the configuration with target plates. The field line traces (followed in both directions) were stopped at the target. White lines: Topology without targets or wall. [Mizuuchi 2001]
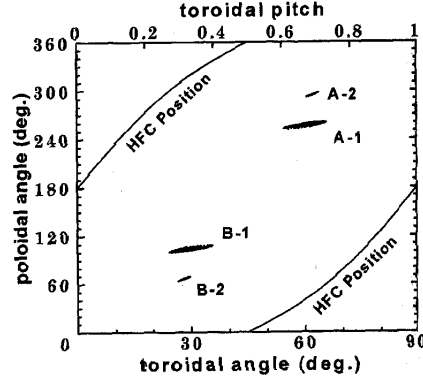
**Figure 3.13:** Footprint locations on the target plate. [Mizuuchi 2001]

The field lines with long $L_c$ seem to be concentrated along the island separatrix side. The long connection lengths are expected to be an advantage for obtaining a large temperature gradient between the SOL and the target plates. Fig. 3.15 shows the distribution of the connection lengths within a 2 cm zone outside the LCFS. The field lines starting near the X-point have longer $L_c$ than those starting near the O-points. The incident angles of the field lines to the target, which are important for the distribution of the heat loads on the target, were found to be less than 10° in the case investigated. In the present Heliotron J one gets for this configuration for $P_{NB}$~1MW and $P_{rad} \sim$ 40% an averaged heat load on the target of about 10 MW/m$^2$. Taking the profile across the footprints into account, the peak heat loads will be even higher. Due to the short pulse lengths of the discharges this does however not pose a problem in Heliotron J.
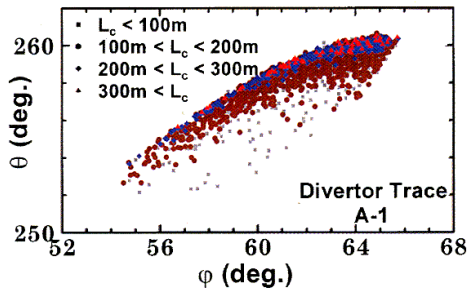


**Figure 3.14:** Connection lengths of the footprint A1 in figure 3.13.Colour code from short to long Lc: grey, brown, blue, red [Mizuuchi 2001]
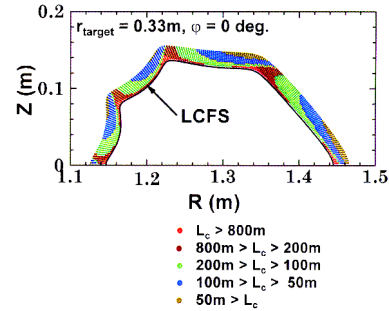
**Figure 3.15:** Field line connection length distribution in a 2 cm zone outside the LCFS. [Mizuuchi 2001]

### 3.3    CHS (Compact Helical System)

On CHS, a l=2/m=8 heliotron/torsatron device, the first Local Island Divertor (LID) experiments have been performed. They provided critical information on the edge plasma behaviour in the heliotron/torsatron device and serve as a guidance for the design of the LID for LHD [Morisaki 1997]. An interesting characteristic of CHS is its magnetic field structure in the edge region. Toroidal effects make the separatrix surface fairly vague. The closed surface region is surrounded by the stochastic structure and no clear separatrix exists.

An LID has been installed on CHS to demonstrate its principle functioning and to study its effects on the edge plasma. It was originally proposed as a means to enhance energy confinement through neutral particle control, i.e. its main purpose is to control neutral particle recycling [Masuzaki 1998]. The advantage of the LID over the closed full helical divertor is the technical ease of hydrogen pumping because the hydrogen recycling is toroidally localised.

The LID is a closed divertor segment with a head shaped to the magnetic flux surface. It utilises an m/n = 1/1 magnetic island, formed in the edge region, as a divertor configuration (fig. 3.16) The separatrix of the m/n=1/1 (pol./tor. mode numbers) island is formed by the perturbation field $B_{LID}$ produced by 8 pairs of circular perturbation coils located above and below CHS. The ration of the perturbation field to the toroidal field was about 0.1 %, and the width of the island was about 5 cm. Little shift of the edge boundary takes place by applying the perturbation field. Li-beam edge density profile measurements show, that too large control coil currents $I_{LID}$ lead to a destruction of the magnetic surface in the edge



**Figure 3.16:** The m/n=1/1 magnetic island geometry and its relation to the LID chamber for O-point operation. The outer edge of the island intersects target plates on the back of the LID head. [Lyon 1997]

region and a widening of the ergodic layer [Masuzaki 1997]. The current in the LID coils can be chosen to position either the O-point or the X-point of the island at the location of the LID head. In the following we will only consider the O-point case since it has much higher exhaust efficiency. Some information on X-point operation can be found in ref. [Lyon 1997].

The divertor head is inserted into the island (fig. 3.16) from a port at the horizontally elongated cross section, where the island width is maximal. The island separatrix provides the connection between the edge plasma region surrounding the core plasma and the back plate of the divertor head through the field lines. The particle flux and the associated heat flux from the core plasma strike the back plate of the divertor head and thus particle recycling is localised in this region. The divertor head is placed into the pumping duct such that the LID forms a closed divertor system with high pumping efficiency (cryogenic pump with a hydrogen pumping speed of 21000 l/sec) for efficient particle exhaust [Masuzaki 1998, Komori 1994].

IR camera pictures of the target area as well as ion saturation current measurements with target integrated Langmuir probes, clearly demonstrated that the particle flow is indeed guided to the back side of the divertor head by the island magnetic field structure, the fundamental function of this type of divertor. The particle flux derived from the probe measurements indicated that the LID pumping efficiency in CHS could be as high as 10 %.
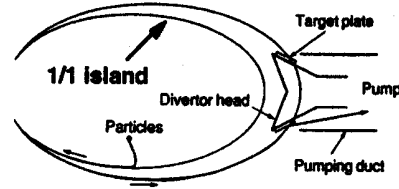
A much higher pumping rate will be achieved in LHD because a majority of plasma flux flowing outwards is expected to be guided to the target plates on the divertor head without diffusing to the wall due to LHD's smaller diffusion coefficient and larger size.

The gap between divertor head and pumping duct was 4 cm. The IR camera pictures showed that the strike points were located ~1cm away from the leading edge of the LID. For the standard LID configuration the leading edges of the divertor head were located well inside the island, thereby being well protected from the outward heat flux from the core (fig. 3.16). This ensures that even at considerably higher input power one doesn't get a leading edge problem.

Neutral pressure measurements with a fast-ion gauge located in the pumping duct directly behind the divertor head indicated that efficient pumping of the recycled neutral particles takes place when the perturbation field $B_{LID}$ for the LID is switched on. This observation is strengthened further by the fact that the $H_\alpha$ radiation behind the divertor head behaves similarly to the neutral particle pressure in the pumping duct [Komori 1997].

The effect of LID operation on edge and core plasma has been investigated by comparing discharges run with $B_{LID}$, to produce the m/n=1/1 island, and without $B_{LID}$.

For the plasma edge it was found that the use of the LID does not lead to a reduction of the edge density near the O-point (Li-beam measurements) despite a factor 2 reduction of <ne>. Moreover $T_e$ above the strike points at the back plate of the divertor head was about twice as large with $B_{LID}$ and the particle flux to the edge of the divertor head was clearly reduced by applying the m/n=1/1 island [Masuzaki 1998].
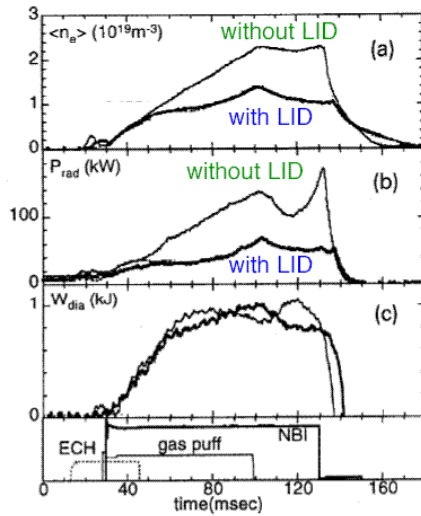


**Figure 3.17:** Typical time evolution of (a) line averaged density (central cord), (b) radiated power, (c) diamagnetic stored energy. The same gas puff rate was applied. [Masuzaki 1998]



**Figure 3.18:** OV line intensity as a function of line averaged density. The stored energy is almost the same for both cases in this density range. [Masuzaki 1998]

LID operation also had considerable impact on the core plasma parameters (fig. 3.17) [Masuzaki 1998]. The core density was reduced by almost a factor 2 compared to non-LID discharges at the same gas puff rate. The core radiation was reduced by a similar factor due to a considerably smaller core oxygen concentration with $B_{LID}$ (fig. 3.18). It was found that $Z_{eff}$ is constant for O-point and X-point operation, independent of the control coil current (fig. 3.19) [Lyon 1997]. At the same time, by activating the LID, the stored energy could be increased by about 20 % compared to a discharge run at the same density (reduced gas puff).
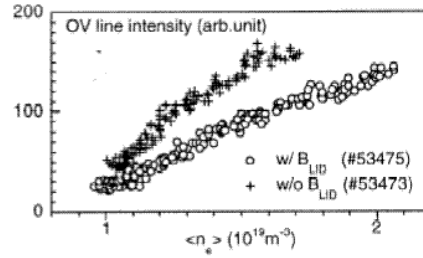
These observations indicate, that the edge plasma changes provoked by the LID configuration have considerable impact on the core plasma parameters. The main role the edge plasma plays in this, is the screening hydrogen neutrals and other impurities. The higher edge $T_e$ led to reduced ionisation lengths and thereby helped to considerably reduce the influx to the confinement region, thereby leading to a lower core density and radiation power. Recycling particles ionised at the outer separatrix region can easily be removed by LID pumping.

Pressure measurements inside the LID chamber suggested that the plasma flux into the LID pump chamber does not affect the flow of neutrals back into the CHS vacuum chamber, i.e. one gets no plasma blocking in the relatively wide channel into the LID pump chamber [Lyon 1997].
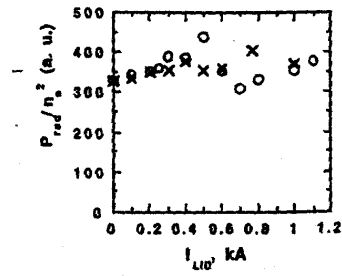


**Figure 3.19:** Prad/ne2 is independent of O- (o) or X-point (x) operation with the LID head in. [Lyon 1997]

## 3.4 LHD

LHD is a superconducting heliotron type device with a pair of l/m = 2/10 (m=toroidal mode number) continuous helical coils with pitch modulation and three pairs of upper and lower poloidal coils, - the inner vertical, the inner shaping and the outer vertical coils [Iiyoshi 1999].

Various innovative divertor concepts have been developed for LHD. Two different divertor magnetic configurations are being explored in LHD, the helical and the island divertor. While the helical divertor utilises the inherent divertor magnetic configuration, the island divertor configuration is enforced by additional control coils (fig. 3.20). Closed divertors, like the LID and
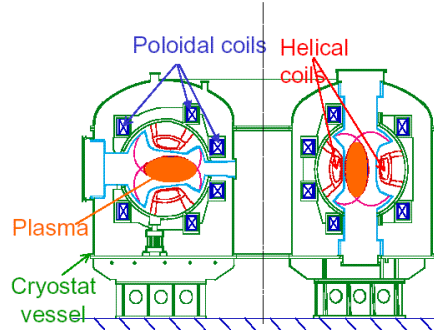


**Figure 3.20:** LHD cryostat and coils [Ohyabu 2001]

the closed full helical divertor, are expected to be equally suitable for high edge temperature low density discharges, due to their high pumping efficiency, and for low temperature and high density radiatively cooled divertor plasmas because of the high plasma plugging efficiency required for high recycling operation [Komori 1994].

### 3.4.1 Magnetic flux mapping

One magnetic flux mapping was performed under steady state conditions at reduced magnetic fields of up to 0.25 T, using a 1 m x 2 m fluorescent mesh. The diameter of the electron beam was less than 3 mm. Closed nested magnetic surfaces which agreed well with the theoretical calculations have been observed. The m/n=1/1 and 2/1 islands caused by the terrestrial magnetic field are only showing up on the measured and calculated surfaces because the magnetic field used for the mapping was very low [Iiyoshi 1999].

A further flux mapping which was carried out at $R_{ax}$ = 3.6 m and at $B_t$ = 2.75 T, showed an m/n=1/1 island with a width of ~8 cm and an 2/1 island with a width of ~5 cm, which seems to be generated by an error field. The cause for such large islands is unclear. Both islands could however be almost simultaneously eliminated by employing the perturbation coil system (fig. 3.21). The accuracy of the thus realised magnetic surfaces was better than what could be expected from the maximum tolerance permitted in the coil specifications [Komori 2001].
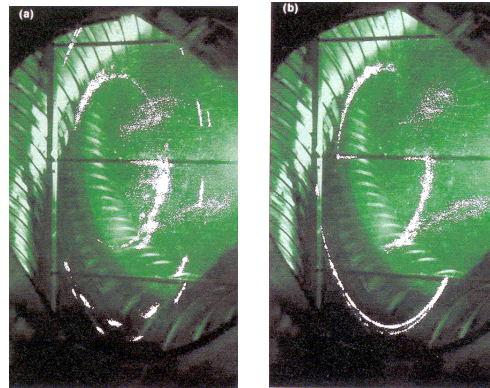


**Figure 3.21:** Magnetic surfaces measured by fluorescent mapping at Bt = 2.75 T and Rax = 3.6 m. (a) without and (b) with compensation by LID coil. [Komori 2001]

### 3.4.2 The Helical Divertor

In LHD the intrinsic helical divertor magnetic field structure forms a clean separatrix, which can be utilised for particle and heat control and for various confinement improvement schemes. The long term aim is to install a closed full helical divertor which utilises the natural separatrix in the edge region (fig. 3.22). This aim is being approached in several steps. In the $1^{st}$ and $2^{nd}$ experimental campaign the divertor structure interacted with the vacuum vessel and divertor strike plates made of stainless steel. This led to a high level of high Z impurities in the plasma core causing a slow (~1s) cyclic oscillation in the plasma parameters during long pulse NBI heated discharges, sometimes described as a 'breathing' plasma [Peterson 2001]. Initial experiments to investigate the divertor plasma properties of the 'natural' helical divertor have already been performed in these stainless steel bounded plasmas [Masuzaki 1999, 2001]. Since the $3^{rd}$



**Figure 3.22:** Sketch of a possible fully closed helical divertor. [Noda 2001]

experimental campaign an open, actively cooled helical divertor is being used (fig. 3.23 and 3.24), which consists of isotropic graphite armour tiles with a copper heat sink, a water cooling pipe and a graphite sheet [Kubota 1998]. The total graphite area amounts to about 30 m$^2$ or 4 % of the total wall surface [Peterson 2001]. This structure is designed for a maximum heat load of 5 MW/m$^2$ for 10 s or 10 MW/m$^2$ for 5 s [Ohyabu 1998].
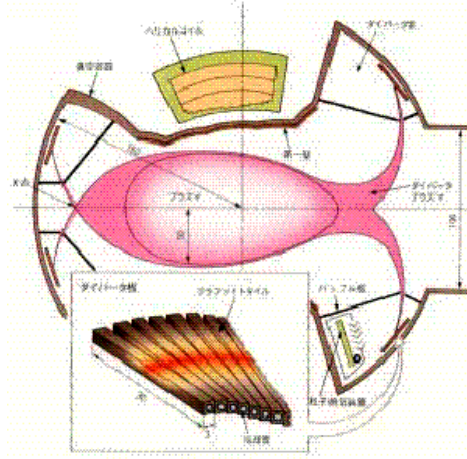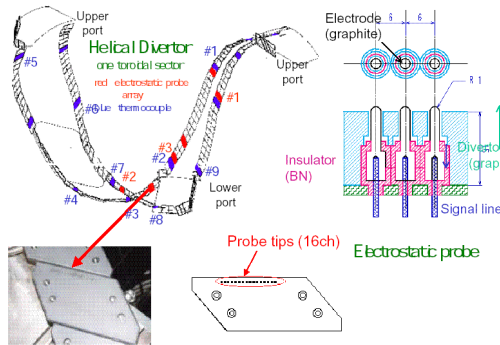


**Figure 3.23:** The divertor structure of one full toroidal sector is shown together with the locations of target integrated diagnostics. [Ohyabu 2001]
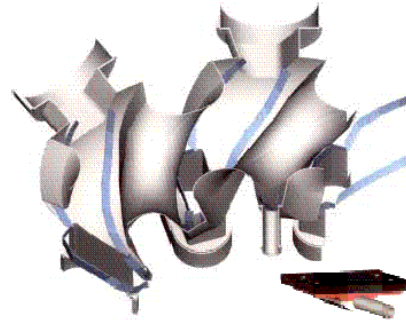


**Figure 3.24:** The blue bands mark the regions along which the divertor target plates shown in fig. 6.3 are running along the torus wall. [Ohyabu 2001]

Experiments have shown that an inward magnetic axis shift of Δ=-0.15 cm results in better confinement, as had been expected from particle orbit calculations [Ohyabu 1994a]. The investigation was limited to configurations with $R_{ax}$ = 3.9, 3.75 and 3.6 m (see fig. 2.3) and with a toroidal ellipticity of 1, since for $R_{ax}$ outside this range the divertor legs would have missed the carbon divertor plates. An inward-shift of the magnetic axis by Δ=-30cm ($R_{ax}$ =

3.6 m), relative to the machine axis at R=3.9 m, has been found to exhibit much better plasma performance than could be achieved with standard configuration ($\Delta$=-15cm, $R_{ax}$ = 3.75 m). A factor of 1.6 enhancement of the energy confinement time over ISS95 was achieved. The new configuration had been expected to have unfavourable MHD properties, based on linear theory, but significantly better particle-orbit properties [Ohyabu 1994a], and hence lower neoclassical transport losses. No serious confinement degradation due to the MHD activities has been observed up to $\langle \beta \rangle$ = 2.4 %. The plasma performance at $R_{ax}$ = 3.9 m was found to be the worst of all three configurations investigated. Suppression of the 1/1 and 2/1 islands with the perturbation coils for $R_{ax}$=3.6 m and $B_t$=2.75 T resulted in a slight increase in $T_e$, $n_e$ and stored energy, suggesting that a magnetic configuration with no island is favourable for plasma confinement.

Fig. 3.25 shows $T_e$ and $n_e$ profiles in the edge open field region, measured for different magnetic axis positions, together with calculated $L_c$ profiles [Masuzaki 2001, Ohyabu 2000]. For $R_{ax}$ = 3.6m the connection lengths between R = 4.66 and 4.84 m are less than 10 m. Such short field lines connecting to the divertor plates cannot approach the core region. Therefore $T_e$



**Figure 3.25:** Te, ne and Lc profiles in the edge open field region along R in the elongated cross section for different magnetic axis shifts. Dashed lines indicate location of the LCFS. [Ohyabu 2000]

and $n_e$ profiles do not extend to this region with short connection length. The measured edge profiles are determined by parallel and perpendicular transport, sources and sinks as in tokamaks. However the transport mechanisms which determine the profiles are much more complicated in the helical configurations with stochastic magnetic field lines, than in X-point divertor tokamaks. The $L_c$ profile clearly determines the $T_e$ and $n_e$ profiles. Moreover the pressure in the edge region is obviously not constant since both $n_e$ and $T_e$ are decreasing with R.

Expected particle deposition profiles along the open helical divertor target plates were derived by 'magnetic field diffusion' calculations for different magnetic axis locations (fig. 3.26). The calculations as well as the experimental observations indicate that the wetting of the targets along the helical direction is not uniform and that the particle and heat deposition profiles are sensitive to the location of the magnetic axis. Particle fluxes and downstream temperatures and densities were measured across the divertor target
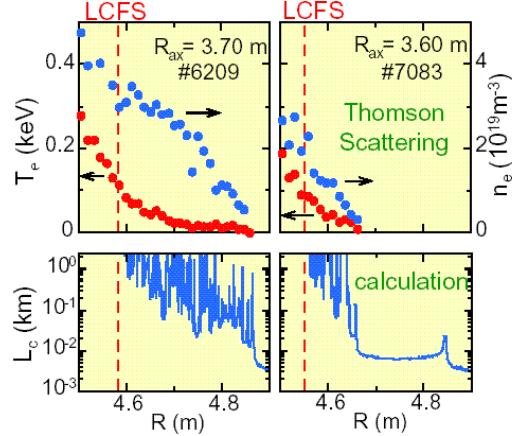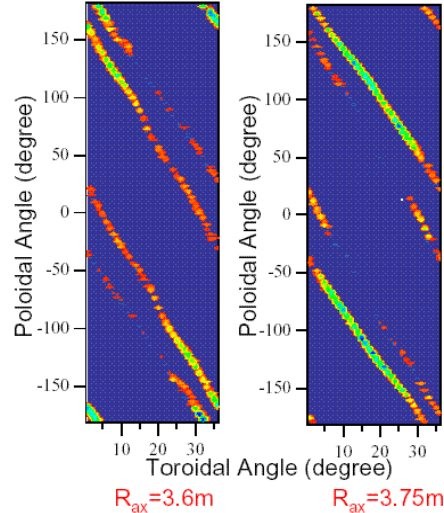


**Figure 3.26:** Particle deposition profiles on the open helical divertor calculated by field line diffusion. [Ohyabu 2001]

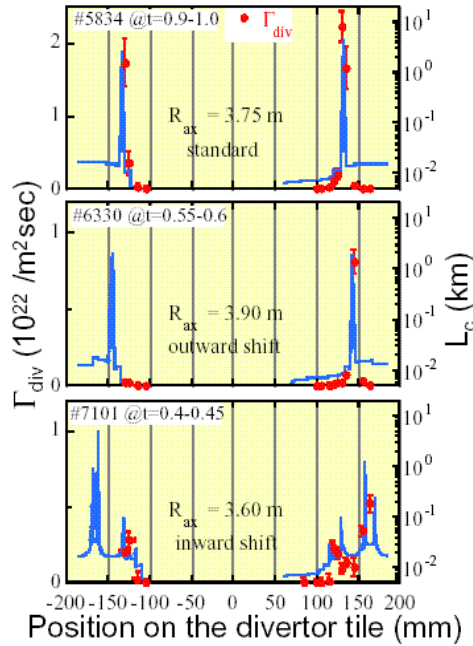plates at different 'toroidal' locations by target integrated Langmuir probe arrays with a spatial resolution of ~6 mm. Measurements of particle flux profiles across a divertor target plate at one location on the inboard side for different magnetic axis positions show that a peaking of the fluxes can, as expected, be observed where the connection length profiles have their maxima, since only field lines with long connection lengths can approach the core region locations (fig. 3.27).

Measurements of upstream and downstream plasma parameters in hydrogen and helium discharges (fig 3.28) show that both densities increase linearly with line averaged density ($n_{ed}$ ~ (1/50) $<n_e>$ in H), while the temperatures are nearly constant or slowly falling with $<n_e>$ ($T_{eu}$~80-100 eV and $T_{ed}$~10-30 eV). The upstream and downstream temperatures and densities indicate that the

**Figure 3.27:** Measured particle flux and calculated field line connection lengths for different magnetic axis locations. [Ohyabu 2001]

electron pressure is not constant in the open field layer due to the collisions and viscosity for the long connection lengths $L_c$.

A non-linear increase in the divertor pressure with increasing line averaged density has been observed in the open helical divertor configuration (fig. 3.29) [Noda 2001]. The absolute pressure, however, was even at $n_e$=6 $10^{19}$ m$^{-3}$ still as low as 3 $10^{-3}$ Pa underlining the necessity of a carefully designed closed divertor, to build up sufficiently high pressures for efficient particle removal.
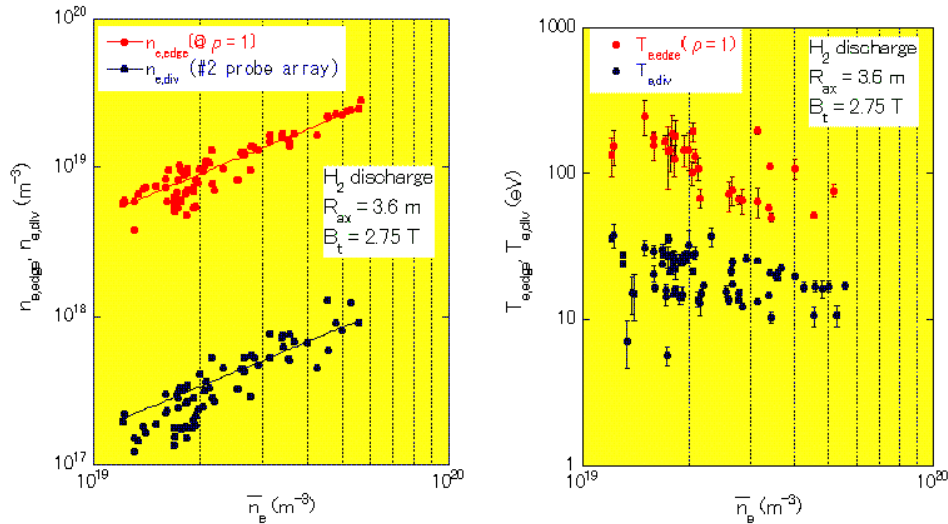


**Figure 3.28:** Upstream and downstream plasma parameters as a function of line averaged density. [Ohyabu 2001]

27

A significant enhancement of the global energy confinement (factor 1.6 over ISS95 [Komori 2001]) has been achieved by the formation of an edge thermal barrier, which exhibits a steep edge temperature gradient [Ohyabu 2000]. The achieved energy confinement times were comparable to ELMy H-mode confinement in tokamaks, however key features associated with the barrier are quite different from those in tokamaks:

- almost no change in particle ( including impurity) transport
- gradual formation of the barrier (not sudden transition into H-mode)
- very high ratio of edge temperature to average temperature $T_{e,ped} / <T_e> \sim 0.7$-$0.8$ (tokamak $\sim 0.2$ in hot-ion H-modes?)
- no edge relaxation phenomena observed (no ELMs)



**Figure 3.29:** Neutral pressure measured in the divertor region during long pulse shots as a function of line averaged density. [Noda 2001]

Well outside the LCFS the plasma density is observed to be as large as 50% of the pedestal density and thus still a considerable fraction of the average density. This means that the particles in this open edge surface layer region are almost confined, which is not too surprising, since cold ions, $T<40$ eV was measured in this multiple surface layer region, are well confined in this region with $L_c > 300$ m. The radiated power remained at about 40% of the deposited power during the steady state part of the discharge and the radiation profile was found to be very hollow and asymmetrically stronger on the outboard side, with the peak emission clearly located outside the LCFS at the location of the pedestal (fig. 3.30) [Komori 1999]).

In the $R_{ax} = 3.6$ m configuration the ergodic and multiple surface layer regions are very narrow (see fig. 2.3a), resulting in a fair overlapping of the high grad $T_e$ and grad $n_e$ regions, which is believed to be favourable for the confinement enhancement. In smaller devices the edge transport barrier was observed, when the LCMS was close to the major rational surface. In the investigated LHD configurations the rational surface or its associated island (m/n=1/1) was always located in the pedestal region, suggesting that they may play some role in the formation of the edge thermal transport barrier. Interestingly however, limiter experiments, in which a carbon limiter



**Figure 3.30:** Time evolution of the radiation measured with a bolometer. [Komori 1999]

head was gradually inserted from ρ=1.2 to 0.8 (fig. 3.31), caused the flux to the divertor plates to fall almost to zero at every position, but did not lead to a destruction of the
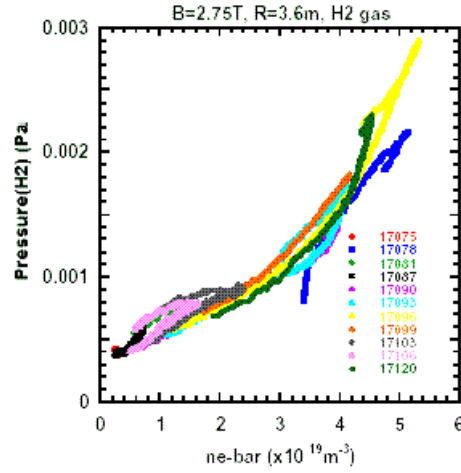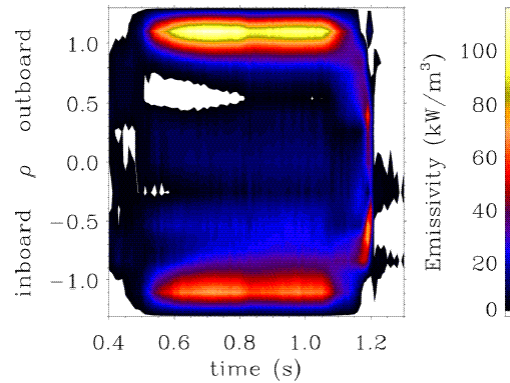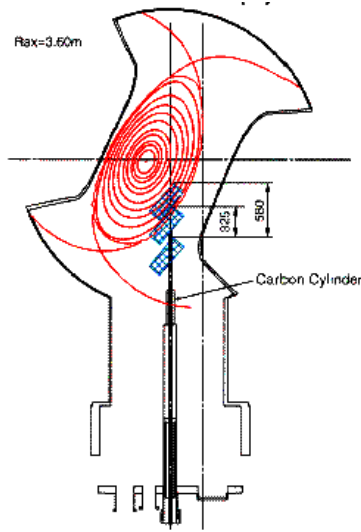
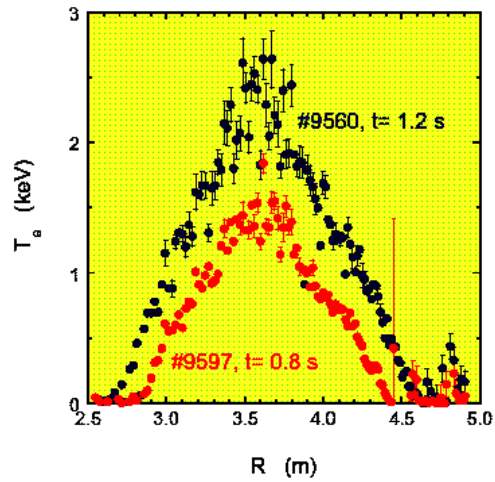**Figure 3.31:** Moveable limiter head. [Nishimura 2001]



**Figure 3.32:** Electron temperature profiles with limiter head moved into (red) and pulled out (blue) of the plasma. [Komori 1999]

pedestal (fig. 3.32), suggesting that neither the ergodic layer nor fairly strong pumping in the edge region (the insertion of the limiter caused an increase in <ne> due to large amounts of gas being desorbed from the limiter when the plasma strikes the limiter) are actually necessary for the formation of the temperature pedestal [Komori 1999, Nishimura 2001]. The temperature gradient at the pedestal remained high and no serious degradation of the energy confinement time was observed (~1.1 ±0.3 of ISS95), i.e. good energy confinement can also be expected in limiter discharges.

The costs of a carbon sheet or membrane pumped closed helical divertor are quite considerable due to the required total length of 40 m x 4 legs. For this reason a simplified closed divertor, which costs an order of magnitude less, has been proposed, consisting of ten 2 m long x 30 cm wide units. The units are located radially slightly inside the X-point and poloidally at the inboard side of the torus (135° < $\theta$ < 225°). Fig. 2.4 showed already the configuration with pumping panels included for HT operation.

### 3.4.3    The local island divertor

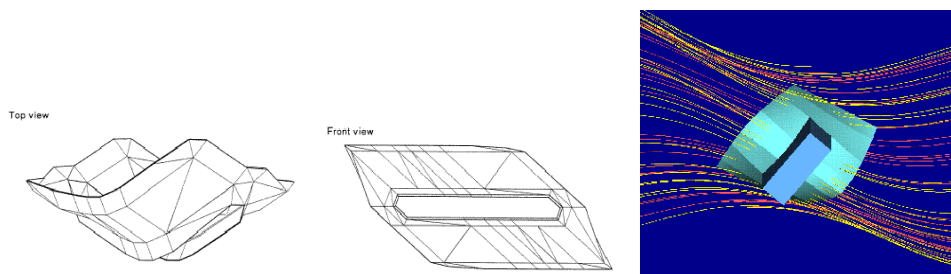20 LID coils (Fig. 2.17), located above and below the cryostat, are installed to control



**Figure 3.33:** Top and front view and a 3D image of the LID head with magnetic field lines. [Komori 1998]

islands and also allow to correct low mode error fields. The construction phase of the LID itself has been preceded by detailed design studies and experimental test on CHS. The divertor head has a size of 1000 x 600 mm (fig. 3.33). It has been designed to take an average heat load of 5 MW/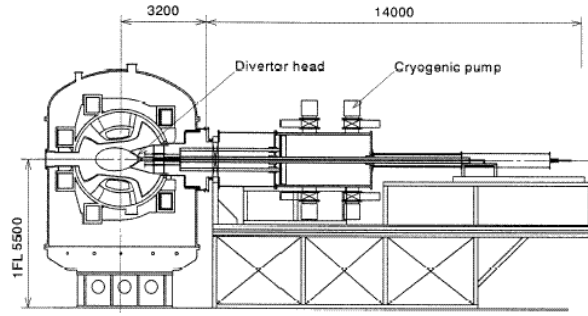m$^2$ during steady state discharges. The main area of the divertor head that receives the particle flux has been designed to be about 0.3 m$^2$ with the angles between the divertor target plates and the particle orbits being less than 10° [Komori 1998, 1998a]. The construction of the vacuum pumping system for the local island divertor was completed in September 2000 (fig. 3.34). This system, which has eight cryogenic pumps with a pumping speed of 42,000 l/s (H$_2$) and one turbomolecular pump with pumping speed of 5,000 l/s, has been used during the fourth experimental campaign as a vacuum system. The LID head is presently being fabricated and experiments with the complete system will start in 2002.



**Figure 3.34:** Design of the complete LID system. [Komori 1998]

First LID configuration tests, without an LID head installed, have already been performed in 1998/99 [Iiyoshi 1999]. An m/n=1/1 island was generated with the LID coils to study the effect that the LID configuration has on ECH plasmas. In the case of configurations with small core plasma volumes ($V_p < V_{p,max}$), the LID configuration led to significant changes in the plasma parameters. The radiation power was considerably reduced while $n_e$ decreased slightly. The stored energy $W_p$ increased significantly , suggesting improved confinement. In the case of configurations with large core plasma volumes ($V_p = V_{p,max}$), however, only little changes in the plasma parameters were observed.

More detailed experiments, without the LID head yet installed, have since been undertaken to investigate the functionality of the LID configuration [Komori 2001]. The effect of the m/n=1/1 island generated by the perturbation coil system on plasma performance has been looked at and compared with that of the intrinsic island, by using the ICRH antennas as limiters by moving them to a location outside the LCFS and just inside the outer ergodic layer. The maximum width of the m/n=1/1 island generated by the perturbation coils is ~15 cm, while that of the intrinsic island is about 8 cm. The
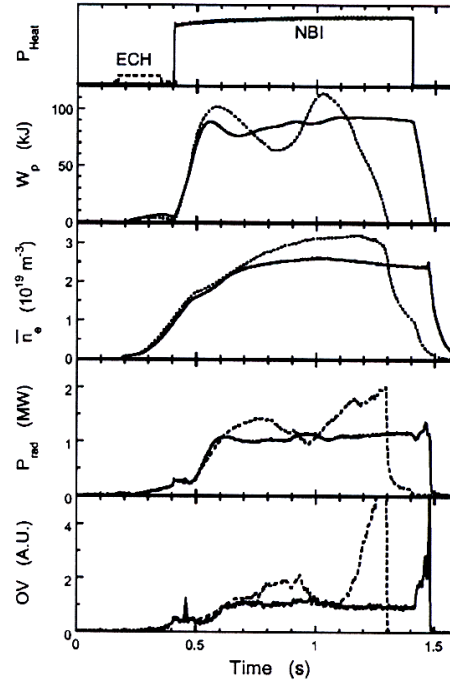


**Figure 3.35:** Time histories of $P_{heat}$, $W_p$, $<n_e>$, $P_{rad}$, Int.(OV) for $R_{ax}$=3.75 m in the standard configuration with the intrinsic island (dotted lines) and the LID configuration (solid lines). [Komori 2001]

most different point between these two configurations is the width of the inner ergodic layer, between the closed flux surface region around the plasma centre and the m/n=1/1 island, which is only a few mm in the standard configuration and ~2 cm for the LID configuration formed by the perturbation coils. The m/n=2/1 islands are the same in both configurations. Fig. 3.35 shows that a much improved plasma performance can already be achieved in this simplified set-up by using the enforced LID configuration, because it prevents impurities from penetrating into the core plasma. While the standard configuration terminates in a radiation collapse, no increase in $P_{rad}$ is observed throughout the entire NBI heating phase in the LID configuration. Bolometer measurements show that in the standard case an intense radiation layer located between $\rho = \pm(0.6\text{-}0.8)$ moves into the core plasma just before the collapse while the LID configuration obviously prevents a weak radiation layer located at $\rho \sim 0.8$ from penetrating into the core plasma. The observed decrease in $\langle n_e \rangle$ is a further expected feature of the LID, which in the preparatory LID experiments performed on CHS has been demonstrated to be attributed to a particle flow along the ergodic layer around the m/n=1/1 island to its back side. The observed variation in $P_{rad}$ in the standard case believed to be due to plasma 'breathing'.

### 3.4.4    Wall conditioning

Wall conditioning on LHD is performed by overnight He (or H) GDC followed by Titanium gettering for 1 hour every morning . Every weekend He GDC is run for 3 days at 95°C baking and boronisation [Livshitz 1990]  is being applied as required [Iiyoshi 1999, Noda 2001].

It is expected that the LID can be used as a means for effective wall conditioning with an input power of 500 kW. One hour of LID cleaning is expected to replace a few weeks of conventional discharge cleaning [Komori 1994].

## 3.5    W7-AS

W7-AS is a low shear, M=5 period modular stellarator with non-planar field coils (fig. 3.36). Within each period the plasma cross section varies from triangular $\Phi=0$ to elliptical ($\Phi=36°$) and back to triangular again (fig. 2.7), such that the field configuration above the horizontal plane over $\phi=0-36°$ is mirror-symmetric to the configuration below the horizontal plane over $\phi=36-72°$,



**Figure 3.36:** W7-AS modular coil system

and vice-versa. The rotational transform can be varied between 0.25 and 0.6 by a set of planar toroidal field coils. By adjusting iota appropriately the 'natural' n/m=5/9 island configuration can be induced, which for W7-AS constitutes the most suitable configuration for divertor operation.
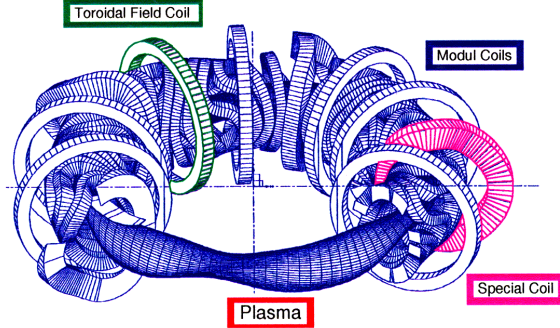
The island divertor concept is presently being put to a realistic test on W7-AS. The strong similarity of the divertor concepts for W7-AS and W7-X make W7-AS an ideal testbed. Initially a set of 10 inboard limiters has been used as a sort of local open divertor structure. In the next step a set of 10 control coils has been build into the machine to gain control over important configurational parameters, like island width, field line pitch inside the island (connection length) and X-point height above the target plate. Following experiments which proved the proper functioning of these coils, a set of 10 discrete divertor modules were installed. This divertor structure is, due to its similarity to the structure envisaged for W7-X, well suited to perform first explorative investigations into the island divertor concept under realistic operating conditions. Moreover these experiments allow for the first time a proper benchmarking of the 3-D transport code ECM3, which has been coupled to the EIRENE neutral gas code.

### 3.5.1    Inboard limiter experiments without control coils

As a first step towards an island divertor for W7-AS, a set of 10 inboard target plates (segmented CFC graphite blocks of 23 cm poloidal and 12 cm toroidal size each) have been
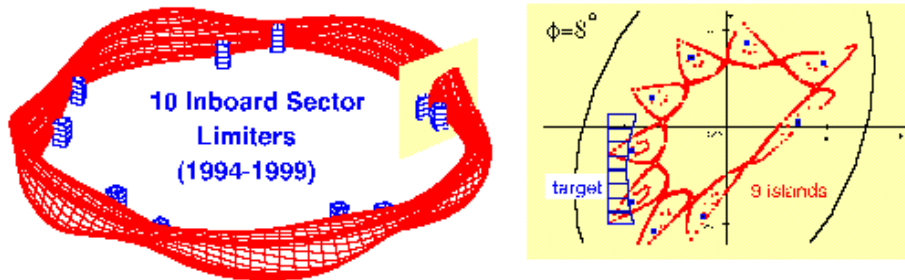


**Figure 3.37:** Configuration of W7-AS with inboard limiters

installed [Sardei 1997]. The X-point height above the target surface could be varied by applying a vertical field which shifts the configuration horizontally outward with respect to the targets. The edge island structure of the 5/8 to 5/11 island chains could clearly be evidenced by the footprints of the island tips on the targets, i.e. by the flux of the recycling particles ($H_\alpha$-light) and by the heat load (calorimetry) across the 8 target tiles of each module (fig. 3.37a and b). Similarly, density measurements with a moveable Langmuir probe array in the triangular plane could confirm the island structure (fig. 3.38d). The maxima of the profiles clearly appear at the intersections of the corrugated island boundary with the target while the minima reflect the usual radial decay of the plasma parameters in a limiter SOL. The phase shift of the island position between resonances with even and odd poloidal mode numbers is well reproduced by the experimental profiles. Since in these experiments the island tips were only just interacting with the targets, while the islands themselves remained well defined and closed, no divertor action could develop in these cases.
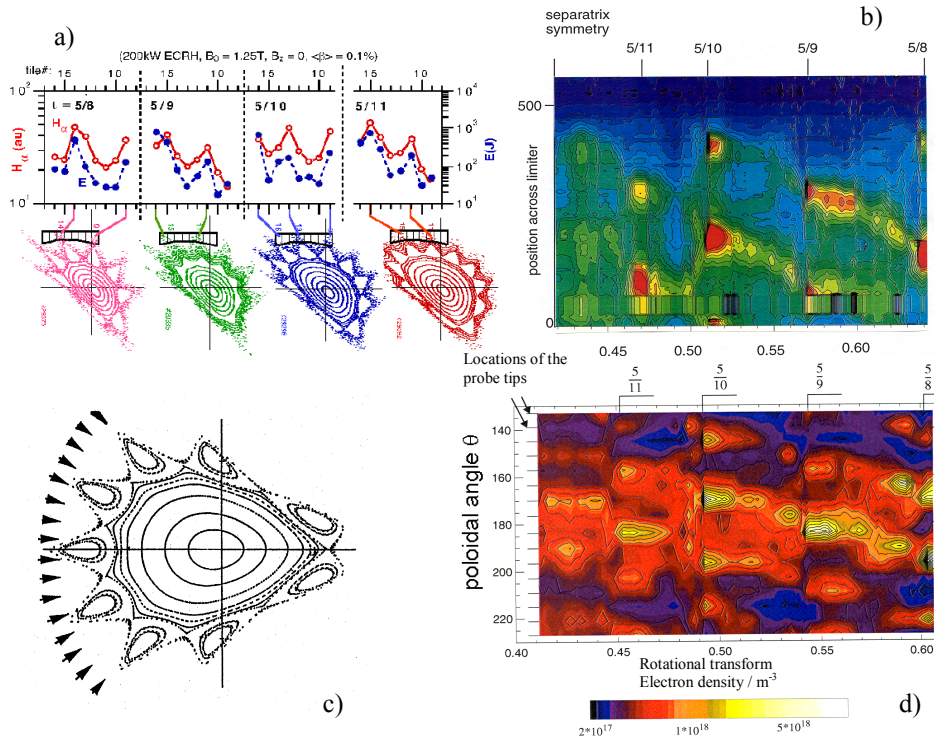


**Figure 3.38:** (a) Particle flux ($H_\alpha$) and energy deposition (target calorimetry) profiles on a target plate for different edge resonances. The profiles peak at the intersections of the corrugated island boundary with the target. (b) $H_\alpha$ profile across a limiter as a function of iota. (c) Arrangement of the probe tips of the moveable Langmuir probe array used to measure the density profile in the triangular plane shown in (d).

As figure 3.38d already indicates one observes in these configurations a poloidal asymmetry of the density contours, i.e. the peak density is for example for the 5/9 island not centred around $\theta$=180° as should be expected. The asymmetry was shown to clearly depend on the magnetic field direction as the two $H_\alpha$ imaged in fig. 3.39 clearly show [König

2001]. Feng et al. [Feng 1999c] have been able to explain the asymmetry in low density plasmas by a poloidal ExB-drift inside the island. Particles diffusing across the separatrix into the islands experience a poloidal electric drift in addition to the parallel motion along the island fans. The drift originates from the radial electric field associated with the radial temperature drop from the separatrix to the O-point: $E=3(T_{esep}-T_{eO})/er_{isl}$, $r_{isl}$ being the island radius at the separatrix. The resulting force then leads to a particle accumulation in the
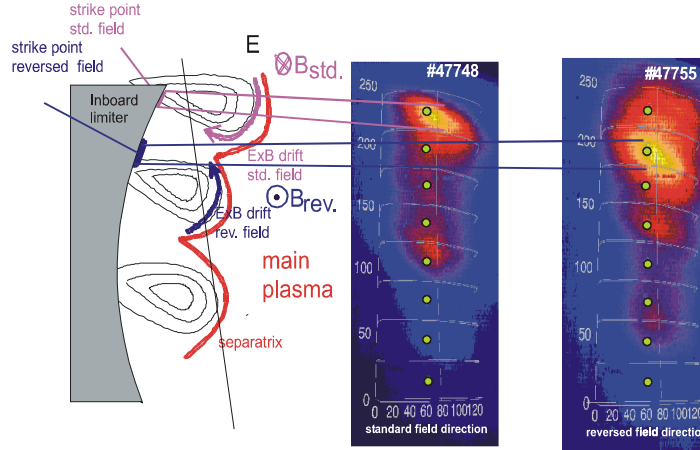


**Figure 3.39:** Effect of the $E_r$xB drift in the island SOL on the strike point location for standard and reversed field operation for two very low density pulses. The green circles indicate the locations of target integrated Langmuir probes. [König 2001 ]

upper or lower island fans, depending on the field direction. By detailed 3-D transport calculations with ECM3 it was possible to reproduce the experimental findings.

The impact of high ß operation on the island structure has been particularly investigated for the divertor relevant 5/9 island configuration [Sardei 1997]. In these experiments the islands were intersected by the target plates like in figs. 2.8 or 3.37, so that divertor fans were being formed along the outer separatrix .$H_\alpha$ images of the strike points clearly showed that the structure and phase of the observed poloidal strike sequence remained locally stable at least up to central $\text{ß}_0$ of ~ 3.7 %, corresponding to <ß> ~ 1.8 %. Equilibrium calculations for $\text{ß}_0$=1% accurately reproduced the strike point locations. These calculations showed that the equilibrium currents lead in this case to a doubling of the field line pitch inside the islands, which implies that the connection length is reduced by a factor 2.

An analysis of high density NBI discharges gave strong indications that high recycling with significant flux enhancement was achieved in this geometry for $n_e > 10^{20}$ m$^{-3}$ and a loss power of 1 MW crossing the separatrix. Fig. 3.40 shows that at <$n_e$> = 1.5 $10^{20}$ m$^{-3}$ the measured downstream density and $H_\alpha$ dropped again, suggesting a rollover consistent with detachment [Sardei 1997, Grigull 1997]. But plasma pressure losses towards the targets were relatively strong and high recycling therefore sets in only at <$n_e$> > $10^{20}$ m$^{-3}$. The resulting density enhancement in front of the targets was only moderate (up to a factor of 3 relative to the upstream density). The observed scenarios were in basic agreement with code predictions. The target integrated Langmuir probe density and the $H_\alpha$ profiles were reproduced satisfactorily by the EMC3/ERIRENE code [Feng 1997] calculations. Density control was generally lost near the time of detachment and the discharges terminated in a radiative collapse. From the comparison of the experiments and code calculations it became
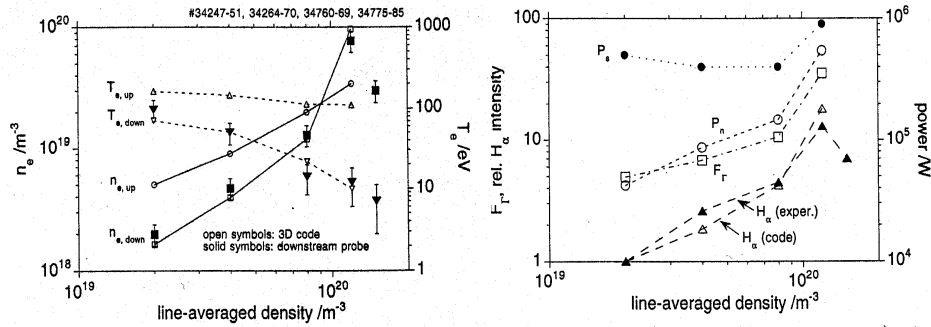
**Figure 3.40:** (a) Upstream and downstream ne and Te values (averaged along the strike line) from EMC3/EIRENE code calculations and experimental downstream data from probe measurements versus <ne>. Local downstream densities from the code were matched to the probe data. (b) Power flow across the LCFS (input for the EMC3/EIRENE code), total power losses due to neutral hydrogen and particle flux enhancement factors $F_\Gamma$ from the code versus <$n_e$>. Calc. and meas. rel. $H_\alpha$ intensities normalised at lowest density. [Grigull 1997]

clear that for further improvements in the divertor performance control coils were needed to gain control over the field line pitch inside the islands and better optimised targets and a more closed structure was required to better focus the recycling neutrals into the islands.

### 3.5.2    Inboard limiter experiments with control coils

As a further step to full divertor operation a set of 10 control coils, two per field period, has been installed inside the machine (fig. 3.41). By varying the control coil current between ±3.5 keV one can change the island width, the core plasma radius and the ratio of island width to connection length. The



**Figure 3.41:** Control coils.

effect the additional field component has depends on the resonant m-number, the radial position of the resonance, on the vertical field and on ß. The proper functioning of the control coils has been confirmed for example by inducing a phase jump in the density structure measured with the Langmuir probe array as a function of the control coil current [Feng 1997]. Furthermore the predicted



**Figure 3.42:** Stored energy and control coil current versus effective minor radius $a_{eff}^2$ at <$n_e$>=1 $10^{20}$m$^{-3}$ [König 2001]

35

change in the core plasma radius as a function of the control coil current could be verified through an appropriate change in confinement (Wdia, Icc showed the expected scaling $\sim a_{eff}^2$) (fig. 3.42) and measured changes of the widths of electron temperature profiles from ECE. Even though it has not been possible to create detached plasmas in the course of the inboard limiter divertor experiments with control coils, nevertheless high recycling conditions could be driven by a combination of high power NBI heating and strong gas puffing. This was necessary to prevent a transition into an ELM-free quiescent H*-mode [Grigull 1999], i.e. to keep up sufficiently high edge densities. The radiation collapse exhibited by ELM-free discharges, essentially defining the density limit, can be ameliorated (or pushed to higher $<n_e>$) by augmented heating power. Additional heating brings with it the synergetic effect of increased $<n_{e,thr}>$ for entrance into the H*-mode (Fig.3.43, for $t_a$ =0.558) as well as increased separatrix densities for a given
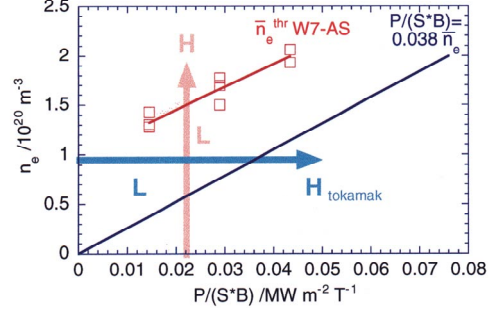


**Figure 3.43:** The route into the ELM-free quiescent H-mode in the W7-AS stellarator is orthogonal to the one in tokamaks. [König 2001]
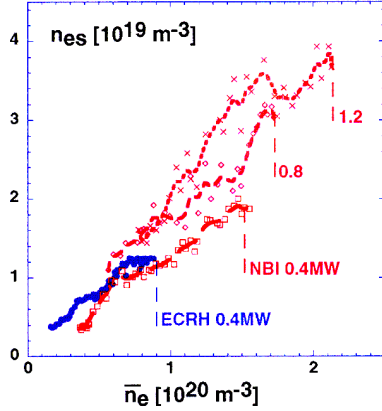
$<n_e>$ (Fig. 3.44). Both effects work in the direction of providing the upstream conditions necessary for a viable high density island divertor. Note, the observed increase in $<n_{e,thr}>$ with $P_{NBI}$ is in direct contrast to tokamak experience, where a power threshold $P_{thr} \sim <n_e> B_t$ is found, i.e. where higher $<n_e>$ necessitates higher power and not vice-versa.

According to fig. 3.44 separatrix densities $n_{es}$ approaching $4 \times 10^{19}$ m$^{-3}$ at $P_{nbi} \sim 1.2$MW can be realised.

As a preparatory measure for future experiments the upper boundary for $n_{es}$ has been explored [McCormick 1999, 2001]. $P_{nbi} > 1.2$MW is necessary to assure suppression of the H-mode. For the following investigations therefore an NBI power of investigations $P_{nbi} = 2$MW was chosen. (The machine was freshly boronised to minimise impurity influx.) The two cases of fig. 3.45 exhibit nearly the same $<n_e>$, but differ in gas puff rates by more than a factor 2. $n_e^{lim}$ at the lower limiter



**Figure 3.44:** Separatrix densities $n_{es}$ vs. $<n_e>$ with $P_{nbi}$ as a parameter. [McCormick 1999]

shows a rapid increase with $n_{es}$, following an $n_e^{lim} \sim n_{es}^2$ characteristic (Fig. 3.46) (which is slower than $n_e^{lim} \sim n_{es}^3$ from the 2-point model), and reaching densities $>1.5 \times 10^{20}$ m$^{-3}$. The upper limiter probe achieves still higher $n_e^{lim}$ - which cannot be documented as $I_{sat}^{lim}$ was constrained by the power supply (fig. 3.46). $T_e^{lim}$ falls under 10eV. The rollover in $n_e^{lim}$ suggests imminent plasma detachment from the limiter. However, it appears more likely to be due to the shift of the hot spot across the limiter and away from the probe as the plasma beta increases. In support of this supposition, the 2D $H_\alpha$ camera does not detect any dramatic increase in radiation - which would normally accompany an approach to detachment. Indeed, it shows the plasma-limiter interaction region moving past the probe, and can even absolutely reproduce the temporal form of $I_{sat}^{lim}$ within better than a factor 2
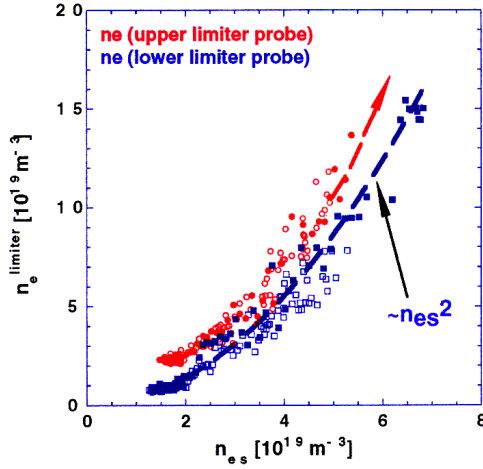
**Figure 3.45:** Peak strike point densities at the upper and lower limiter from Langmuir probes for discharges of Fig.7.10. The arrow indicates still higher densities at the upper limiter, which however cannot be documented due to power supply limitations. [McCormick 1999]

(using $n_e$ and $T_e$ of the probe to estimate the photons/ionisation coefficient). Further, at the $I_{sat}^{lim}$ rollover, no concomitant decrease in power to the limiter is seen by the IR camera.

$n_{es}$ is independently determined from the RCP and the edge Thomson scattering system. The continuous traces of $n_{es}$ of fig. 3.46 come from the Li-beam, whose separatrix position is calibrated by averaging the results of Thomson scattering and the RCP.

For these high power scenarios of short duration, $P_{rad}$ is not a problem. $P_{rad}/P_{abs}$ approaches 30-50 % at the end of the discharges (fig. 3.46), yielding $P_{sol} < 1MW$. The power deposited on the limiters yields $P_{lim}^{total}/(P_{abs}-P_{rad}) \sim 45$-50% from 0.1sec onwards.



**Figure 3.46:** $\langle n_e \rangle$ for two discharges (#47128, 47129) with the gas puff program as indicated. $n_{es}$ from the Li-beam (continuous traces), RCP (dots) and edge Thomson scattering (squares). $n_e$ and $T_e$ at the lower limiter from a Langmuir probe. The upper limiter probe exhibits higher $I_{sat}$ (ergo->higher $n_e$, not shown), but is finally limited by the power supply. $P_{nbi}=2MW$, $P_{abs}\sim1.8MW$, $P_{rad}(0.3s)/P_{abs} \sim 30$-50%, respectively. The electron fuelling rate from NBI is $\sim2.5\times10^{20}$ s$^{-1}$. $H^0 \to D^+$. [McCormick 1999]

Although the result can be only approximate (due at least to the known up-down and toroidal asymmetries), it indicates that a substantial portion of the power is not intercepted by the limiters and lands on other plasma-facing components. Effects of such order are actually expected from field line tracing calculations, meaning the inboard sector limiters are not completely effective with boundary island configurations.

$\langle n_e \rangle$ greater than two times the Greenwald density $n_{e,GW}$ [Greenwald 1988] is attained within these ramped, L-mode discharges. $n_{e,GW}$ obviously does not constitute a principal operational limit.

In the high density divertor discharges it was possible to show that the ratio of cross field to parallel transport can be affected via the control coils. If one assumes particle and momentum transport to be governed by parallel classical convection with a sound speed $c_s$ and a perpendicular anomalous diffusion described by a diffusion coefficient D, then the parallel and perpendicular transport time scales can be roughly estimated as $\tau_\| = L_c/c_s$ and $\tau_\perp = 2r_i^2 / D$ with $r_i$ being the island radius , $L_c = R\pi/\Delta\iota_i$ being the field line
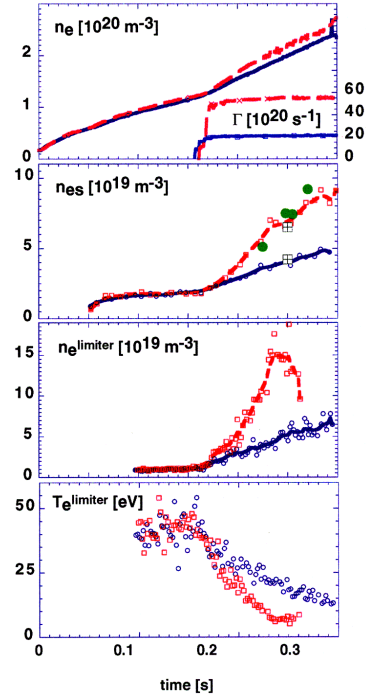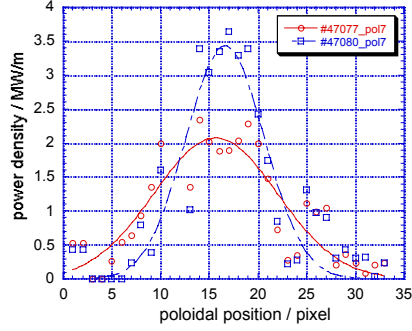
**Figure 3.47:** Broadening of the power deposition profile with increasing connection length $L_c$. #47080: $L_c = 60$ m; #47077: $L_c = 110$ m [König 2001]

connection length measured from the stagnation point to the target, and $\Delta\iota_i$ being the internal rotational transform within an island [Feng 1999b]. With the control coils it was possible to change the ratio of parallel to cross- field transport $\tau_\parallel$ / $\tau_\perp \sim L_c$ / $r_i^2$ by a factor of 1.8 by increasing the connection length $L_c$ (averaged over the strike point region) from 60 m to 110 m by reducing the control coil current from $I_{cc} = -3.5$ kA to 0 kA at a fixed X-point height of 3 cm above the inner limiters. The longer $L_c$ did result as expected in a broadening of the power deposition profile derived from IR camera observations (Fig. 3.47) and a widening of the $H_\alpha$ emission profiles.

In summary these preparatory experiments for the experiments with proper divertor modules had successfully shown, that, at least transiently, edge conditions necessary for a predicted detachment with the divertor modules could be reached. For an $\iota_a = 5/9$ configuration, in conjunction with the divertor modules, and $P_{sol} \sim 1$MW the 3D EMC3 code had predicted that $n_{es} \sim 10^{20}$m$^{-3}$ would be necessary to achieve detachment at the target plates, a value which was clearly in the range of these experiments [McCormick 2001].

### 3.5.3    W7-AS Divertor Operation

For its last operating campaign, W7-AS has been equipped with a set of 10 discrete divertor modules in order to experimentally evaluate the island divertor concept (fig. 3.48).   The divertor modules are placed at the top and bottom of the elliptical cross sections. Appart from the absolute dimensions, the geometry strongly resembles the divertor modules that
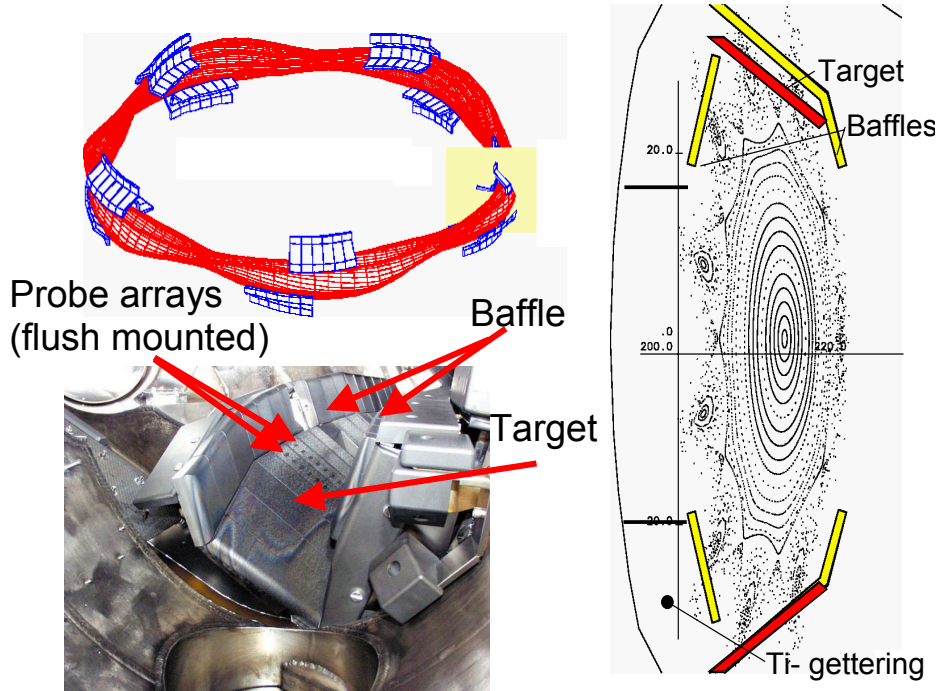


**Figure 3.48:** (a) Arrangement of the divertor modules. (b) Poloidal cut though the symmetry plane. (c) Divertor module inside the machine.
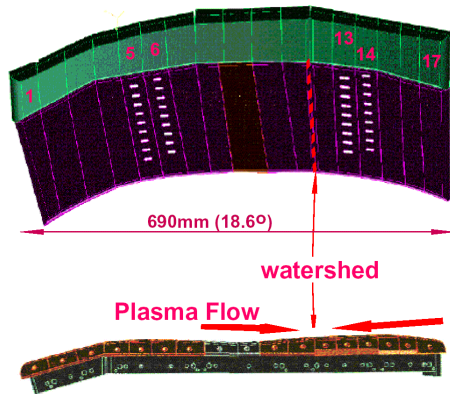


**Figure 3.49:** Outer baffle (green) and target plate with 4 rows of flush-mounted Langmuir probes indicated. An up-down module pair is equipped in this fashion. The two darker tiles (8 & 9) are recessed to avoid leading edge problems in order to accommodate diagnostic penetrations through the target.

will be installed in W7-X. The modules consist of inertially cooled CFC targets and of baffles made of isotropic graphite. The targets are three-dimensionally shaped in order to achieve nearly homogeneous thermal load distributions in the helical direction for the 5/9 island configuration (fig. 3.49). The chambers behind the slits separating the target and inboard baffles are toroidally closed and are equipped with titanium evaporators for gettering of neutrals. The conductance of the opening is about $10^4$ l/s for $H_2$ and the total pumping capacity of all modules is

~5000 l/s corresponding to ~$10^{20}$ particles per discharge at a divertor neutral pressure of $10^{-3}$ mbar [Niedermeyer 2000]. Fig. 3.50 shows the range X-point heights above the target plate and the field line connection lengths principally accessible by varying toroidal, module and control coil currents. This parameter space still needs to be explored in the running campaign, but one has to keep in mind that the X-point distance can only be increased at the expense of the plasma minor radius. The present optimum 'standard' configuration is marked by a star. It has a connection length of $L_c \approx 100$ m at a X-point height of $D_x = 4$ cm. The poloidal width of the 5/9-island is ~5 cm and its radial width ~10 cm. The results that will be reported on in the following were all produced in this configuration [Grigull 2001].
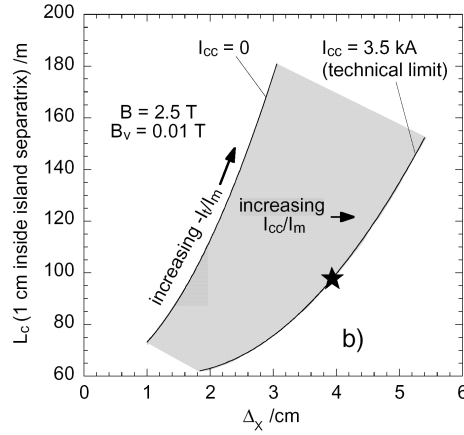


**Figure 3.50:** Field line connection lengths 1 cm inside the islands versus X-point height above the target at various It/Im and control coil currents Icc. The shaded area depicts the accessible operating space which could be further extended by reducing the main field strength. The star marks the present optimum configuration which is reported on here.

### 3.5.3.1 Geometry studies

By calorimetric measurements in low density, high power ECRH discharges it could be demonstrated, that the energy deposited on the individual modules did not scatter by more than 20 % from the average value, which is considered an acceptable symmetry. A comparison of measured (probe arrays and $H_\alpha$ camera images) and calculated strike point locations in low-ß discharges gave satisfactory agreement over a wide range of edge $\iota$ values. A slight top/bottom asymmetry was observed at high $\iota$. Is was found to depend on the field direction which indicates that drifts might be involved. The point will be closely addressed in the upcoming experiments. The locations of the strike points were fairly resilient against ß increases (so far studied up to <ß> ~1%) [Gardelmeier 2001] as had already been seen in earlier investigations on the inboard limiters for <ß> up to 1.8% (see chap. 3.5.1).

### 3.5.3.2 Plasma Performance of High Density Discharges

The new island divertor gave access to a completely new Ultra High Density (UHD) operating regime, which at high power NBI heating benefited not only from considerably improved confinement properties but also from access to a favourable divertor operating scenario [Grigull 2001]. In the UHD regime full density control could be maintained over many energy confinement times and the plasma parameters can be quasi-steadily maintained under attached as well as detached conditions. In this initial study only a single configuration will be reported on, which was found to combine all the above favourable qualities. Systematic exploratory studies of the configuration space will be undertaken in the remaining operating time of W7-AS.

Previous high NBI power limiter discharges used to have rather long particle and impurity confinement times up to the maximum accessible line averaged density of <$n_e$> ~2·$10^{20}$ m$^{-3}$.

The high upstream separatrix densities $n_{es}$ necessary to get access to favourable divertor conditions were difficult to achieve in these limiter discharges, since $n_{es}$ did only rise less than linearly with the line averaged density ($n_{es} \sim <n_e>^\alpha$, $\alpha<1$). Moreover divertor conditions could only be transiently reached, since one had no control over the density in these discharges. Typically density and radiation did rise until the discharges collapsed.

### 3.5.3.2.1  Operation in the UHD regime under attached conditions

Under attached conditions a rather low level of core radiation (O, Cl, Fe) could be quasi-stationary maintained. While the total radiation losses were typically ~25% of $P_{NBI}$(absorbed), only ¼ thereof was radiated from the plasma core. Tomographically reconstructed bolometer profiles show that most of the energy was radiated from a region well outside the separatrix and close to the wall (fig. 3.51).



**Figure 3.51:** Example of an attached quasi-steady state NBI heated discharge at very high density. c) Able inverted radiation profiles from a 32-channel bolometer camera in the triangular plane.

Since only a single configuration has been studied in detail, the line averaged density $<n_e>$ could be used as the key control parameter. In this configuration one has full control over the density, i.e. any density level could be set by appropriate, usually rather low, gas puffing and sufficient neutral beam heating ($P_{NBI} \leq 2$ MW), and quasi-stationary maintained up to a density of $3.2 \cdot 10^{20}$ m$^{-3}$. In the attached regime the improvement in plasma performance takes place in the density range from 1-$2 \cdot 10^{20}$ m$^{-3}$. With increasing line averaged density $<n_e>$ the energy confinement time rises steeply by factor 3 to a level of twice ISS95 [Stroth 1996]), while at the same time the impurity confinement time falls sharply. In the remaining part of the explored density range, i.e. between 2 and $3.5 \cdot 10^{20}$ m$^{-3}$, the energy confinement time gradually saturates, while the impurity confinement time continues to drop linearly with $<n_e>$ (fig. 3.52a).This favourable density dependence of $\tau_{imp}$ in the UHD regime is in clear contrast to former experiments at lower densities, which yielded a $\tau_{imp} \sim n_e(0)^{\frac{1}{2}} P^{0.8}$ scaling [Burhenn 1995, 1997].
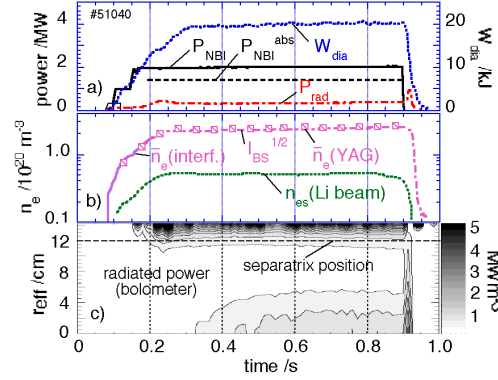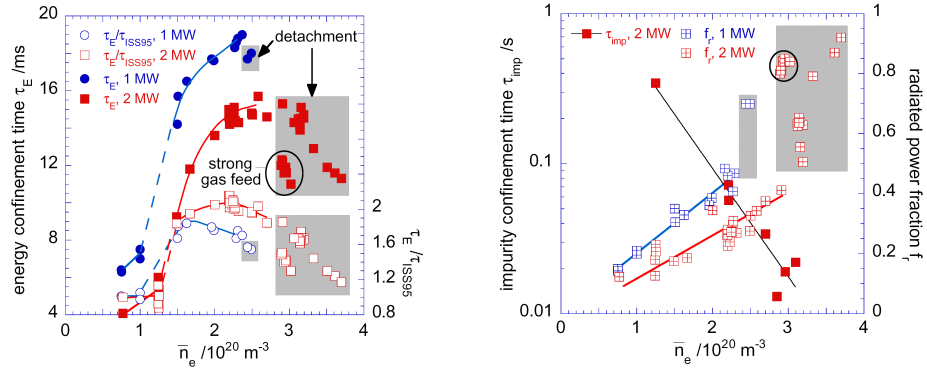


**Figure 3.52:** Energy (a) and impurity (b) confinement times and radiate power fraction (b) as a function of the lines averaged density for NBI heated discharges. The shaded areas indicate partially detached states.

The power losses due to radiation from outside the divertor (the divertor radiation losses could not yet be experimentally quantified) increase linearly with $<n_e>$ (slope $\sim 1/P_{NBI}$) up to a maximum of $P_{rad}/P_{NBI}(abs) \sim 40 \%$ (fig. 3.52b).

In the attached state of the UHD regime the upstream density $n_{es}$ behaves quite differently from previous limiter experiments (see above). $n_{es}$ increases more than linearly with the line averaged density $<n_e>$ ($n_{es} \sim <n_e>^\alpha$, $\alpha > 1$) and even stronger with increasing NBI heating power but clamps abruptly well below densities which lead to a transition to a detached state at a given heating power (fig. 3.53a). For $P_{NBI} = 2$ MW the upstream density was found to clamp at $6.4 \cdot 10^{19}$ m$^{-3}$ for $<n_e> > 2.5 \cdot 10^{20}$ m$^{-3}$. The top/bottom averaged neutral pressure in the divertor sub-volume showed the same linear $<n_e>$ dependence as the



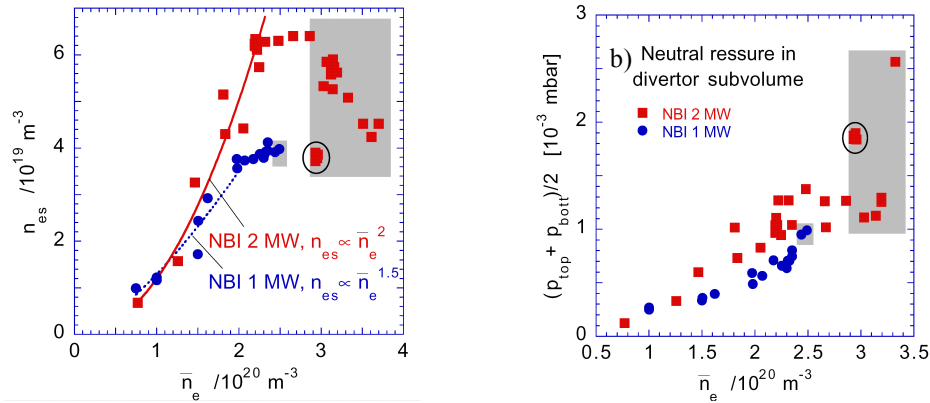**Figure 3.53: (a)** Upstream densities measured at the separatrix position (Li-beam). The upstream density saturates above $<n_e>=2.5 \ 10^{20}$ m$^{-3}$ for $P_{NBI}=2$ MW and drops in the detached regime. **(b)** Neutral pressure measured in the divertor sub-volume (averaged over top and bottom module) versus $<n_e>$. The values reached at high density are expected to be sufficient for active particle pumping by Ti gettering in W7-AS.

upstream density [McCormick 2001], it clamps for $P_{NBI} = 2$MW at a pressure of $\sim 1.3 \cdot 10^{-3}$ mbar for $<n_e> > 2.5 \cdot 10^{20}$ m$^{-3}$, a value believed to be sufficient for active particle pumping by Ti gettering.

### 3.5.3.2.2            Operation in the UHD regime under detached conditions

**a)   rollover**

By pushing the line averaged density up to values above $2.5 \cdot 10^{20}$ m$^{-3}$ ($P_{NBI}=1$MW) or $3 \cdot 10^{20}$ m$^{-3}$ ($P_{NBI}=2$MW) it is possible to combine good confinement properties with the advantages of a detached plasma operation. At these densities the plasma



**Figure 3.54a:** Observation geometry for measurement of C II radiation layer in fig. 8b. (Te contours for illustration only.)
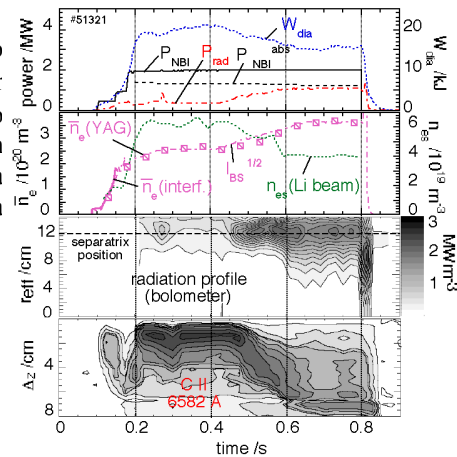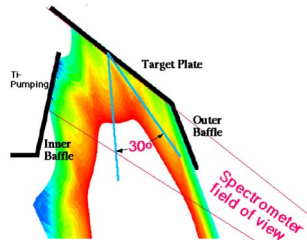
**Figure 3.54b:** Controlled transition to strong partial detachment. The radiation remains peaked at the edge while the low temperature C II radiation layer slowly moves up from the target ($\Delta z=0$ cm) to the X-point at $\Delta z \sim 8$ cm at this poloidal plane (target tile 9 in fig. 3.49).

begins to locally detach from the target plates over most of the divertor area. The transition from an attached to a partially detached regime is a process which can be stepped through gradually in a controlled way by slowly ramping up the density. Experiments were for example performed in which this period was stretched out over ~200 ms, by gradually ramping up the density from a first plateau at $<n_e> \sim 2.5~10^{20}~m^{-3}$ to a second one at $<n_e> \sim 3.5~10^{20}~m^{-3}$ (fig. 3.54b) A high spatial resolution spectrometer ($\Delta z$=9cm are imaged onto the entrance slit of the spectrometer fig. 3.54a) clearly shows the low-temperature C II radiation front (width 1-2 cm) gradually moving up from close to the target surface in the attached phase to the X-point/separatrix location in the course of the density ramp-up. The upward movement of the radiation front is also seen by the divertor bolometer cameras (not shown). The bolometer profiles, being measured in the triangular plane, i.e. toroidally at the symmetry plane between two divertor modules, also indicate a steep rise in radiation near the separatrix when moving towards detachment (fig. 3.54b).

The evolution of the detachment across the target surface was followed by 2-D CCD cameras in the light of $H_\alpha$, $H_\gamma$ and C II [Wenzel 2001], by a 2-D infrared camera and 4 rows of flush mounted target integrated Langmuir probes. The systems show, due to the three-dimensionality of the scrape-off layer (SOL) and the resulting necessity of a 3-dimmensionally shaped divertor structure, which needs to be compatible with a host of different magnetic configurations, a rather complex



**Figure 3.55:** $H_\alpha$ traces on the divertor targets. Tile numbering as in fig. 3.49. The 'watershed' denotes the region closest to the main plasma, i.e. in either toroidal direction the distance to the main plasma increases. Regions A and D show different behaviour with respect to rollover and detachment.

structure of interaction zones which mainly concentrate in two helical stripes across the target area for the configurations reported on here.

On the targets one can define two regions A and D which behave rather differently. The detachment region D, which includes the watershed (location closest to the main plasma and therefore with the highest heat load) typically stretches out from tile 8-16 while in region A (tile 3-7) which includes tile 5 and 6 where the field lines have the steepest inclination, the plasma always remains attached. In the 3-D images the transition to detachment manifests itself in a rollover of the $H_\alpha$ intensities (particle fluxes) and a clear drop in the power load deposited on the target

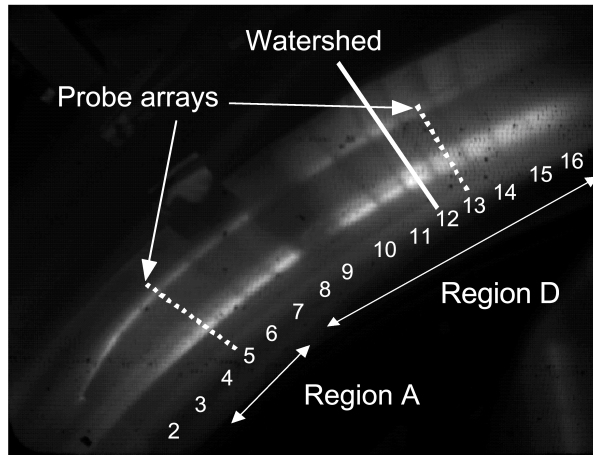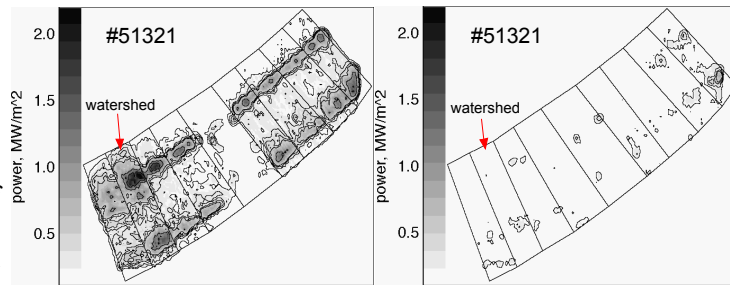

**Figure 3.56:** Images of the bottom divertor taken with a thermography camera showing the change in the power load distribution during the attached (left, t=0.35 s) and the detached (right, t=0.65 s) phase of the discharge shown in fig. 3.54b.

(thermography). Only in region A an attached zone always remains albeit with considerably reduced power load. The detailed analysis of the transition to the detached state was restricted to the location of the flush mounted Langmuir probes of which one poloidal row was located just where the plasma always remains attached. The downstream measurements there where complemented by upstream measurements with the Li-beam and the edge Thomson scattering system.

On the route to detachment the rollover in the particle flux onto the targets (derived from $H_\alpha$ intensities and ion saturation current on the probe arrays on tile 5 and 13) sets in when with increasing density $\langle n_e \rangle$ the upstream separatrix density $n_{es}$ and the divertor sub-volume neutral pressure clamp (fig. 3.53). The threshold value at which the upstream density $n_{es}$ clamps, was found to scale with the net power $P_{loss}$ flowing across the separatrix into the SOL (fig. 3.57). The downstream temperature on tile 13 at the density where $n_{es}$ clamps is, compared to similar observations in tokamaks, rather high (> 10 eV). In this temperature range the momentum losses by CX neutrals are not adequate to explain the observed loss of parallel momentum, which manifests itself in the observed rollover of the particle



**Figure 3.57:** Upstream separatrix densities (from Li-beam) at the point where the particle flux onto the targets in region D of fig. 3.55 begins to decrease with increasing line averaged density ('rollover') (fig. 3.53a). Also shown are the corresponding downstream temperatures at the location of the maximum of the downstream density profile across the strike points (from probe array at tile 13). The upstream density at rollover scales with the loss power.

flux to the target. It is rather the predicted high cross-field transport associated with the specific island geometry (see near end of chapter 2.2), which seems to play a role here.
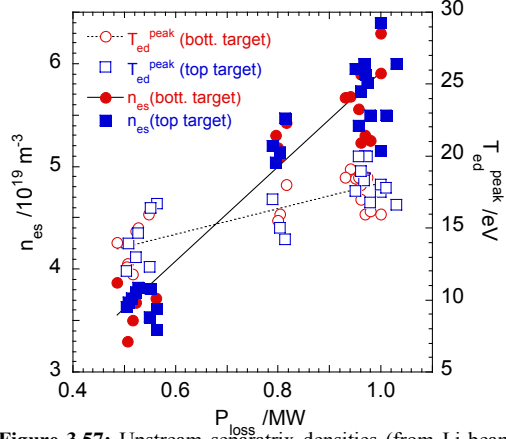
**b) detachment**

Measurements on tile 13 (representative for target region D) show that by increasing $\langle n_e \rangle$ past the rollover point, the downstream parameters continue to drop until finally partial detachment sets in when $n_{ed} \sim 0.5\text{-}1 \cdot 10^{19}$ m$^{-3}$ and $T_{ed} \sim 10$ eV are reached at $P_{NBI} = 2$ MW (fig. 3.58a). Both divertors, the top and bottom, behave rather similarly, the differences being within the error limits, i.e. in region D the plasma detaches simultaneously in both, the upper and the lower divertor module. This observation is in agreement with $H_\alpha$ camera observations from both modules. Due to the fact that $n_{es}$ no longer increases with $\langle n_e \rangle$ once the maximum value of $\langle n_e \rangle \sim 2.5 \ 10^{20}$ m$^{-3}$ has been reached (see fig. 3.53a), the downstream values as a function of $n_{es}$ exhibit a steep drop after rollover (fig. 3.58b). Prior to rollover $n_{ed}^{peak}$ increases linearly with $n_{es}$; rollover sets in where $n_{es}$ becomes constant. It is important to note here that $n_{ed}$ never exceeds $n_{es}$, and this holds also for the other probe array positions, indicating that detachment is achieved without running through an intermediate high recycling regime. Moreover the maximum downstream temperatures, which were found at the same location as the peak densities, remain fairly high compared to the detachment conditions one is used to in tokamaks. No indication of volume recombination has been found, neither in the $H_\alpha/H_\gamma$ images of the lower divertor nor in the
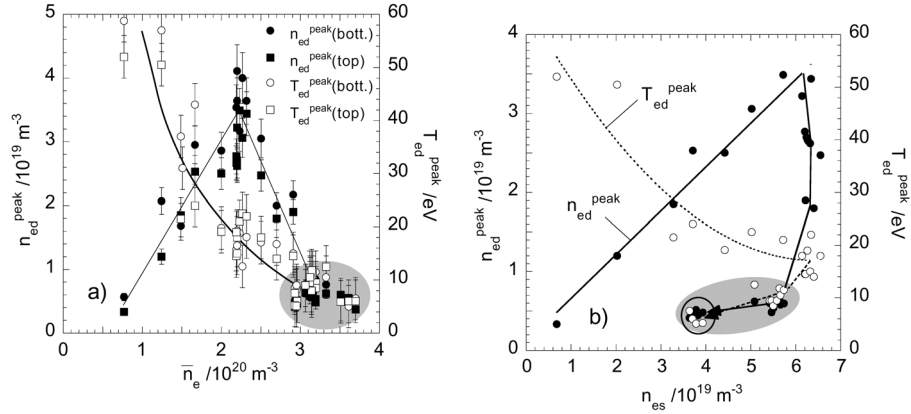
**Figure 3.58:** 2 MW NBI discharges. Shaded areas indicate detachment from region D. **(a)** Peak downstream densities and temperatures at tile 13 (representative for target region D; in top and bottom module) versus line averaged density. (b) Peak values, i.e. values at location of maximum density, at tile 13 (top divertor module) versus upstream separatrix density. The lines are guiding the eyes and indicate the development towards detachment.

Balmer series spectra observed between target and separatrix with the spectrometer set-up depicted in (fig. 3.54a) at the upper divertor. These observations clearly indicate that the temperatures at detachment remained above 2 eV. The detachment is partial in the sense that a finite but much reduced particle flux remains, the power load on the target is strongly reduced and the downstream temperatures remain above 2 eV.

The situation in zone A, studied in detail on tile 5, is rather more complicated. At line averaged densities at which the plasma clearly detaches in zone D, one finds in zone A a bifurcation in $T_{ed}^{peak}$ and on the top target also in $n_{ed}^{peak}$. (It should be noted here, that only on the bottom target (fig. 3.59b) the location of the peak temperature does not coincide with the one of the peak densities.) A complex interplay between top and bottom targets which changes with density and strength of the external gas feed is observed. Depending on the latter, two scenarios can be distinguished. At the upper target (fig. 3.59a), strong gas feed leads, for conditions at which the plasma detaches from region D (grey shaded area), to decreased downstream densities and increased temperatures, whereas with weak gas feed
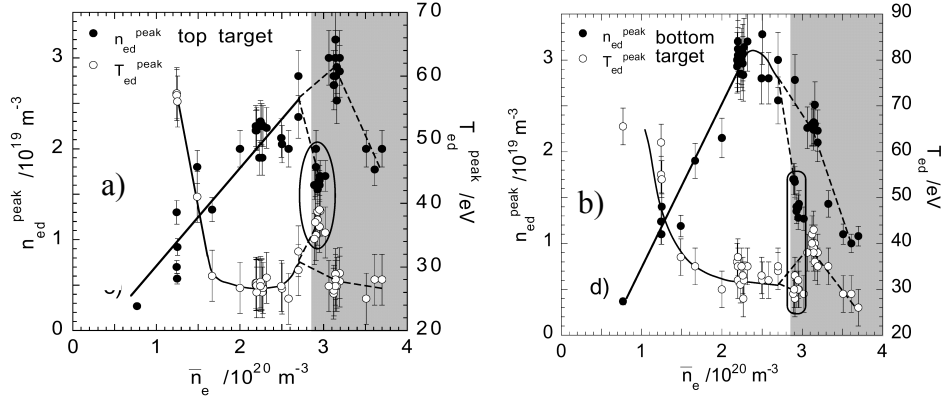


**Figure 8.12:** 2 MW NBI discharges. Downstream peak plasma parameters at tile 5 (representative for region A). The shaded areas mark the density range of <ne> within which the plasma detaches in region D. The plasma does however not detach in region A for which the data are shown here and there is clearly a top/bottom asymmetry.

the density remains high and the temperature becomes slightly lower. At the bottom target (fig. 3.59b) the temperature shows the inverse behaviour, whereas the density drops sharply in both cases. The plasma always remains locally attached in region A, even at the highest densities. The fact that at all probe positions $n_{ed}$ never exceeds $n_{es}$ is a strong indication that in the island divertor configuration investigated here, detachment is reached in a, compared to the situation in tokamaks, rather unusual way, that means without running through an intermediate high recycling regime. The observed strong reduction in the power load onto the targets in the detached state is largely due to the significant radiated power fraction (divertor radiation again not included) , which rises from ~ 25% in the attached to ≥ 80% of $P_{NBI}$(abs) in the detached phase (fig. 3.54b). Inverted bolometer profiles (not including the divertor) show that the investigated strongly detached plasmas radiated most of the power from a zone close to the separatrix. In the divertor region the C II and C III



**Figure 3.60:** Spatio-temporal evolution of the C II radiation layer. L.o.s. see fig. 3.54. Distance denotes the vertical height above the target. (a) #51040: attached (radiation layer remains at target), (b) #51050: detached (radiation layer stabilises at a location between target and separatrix and (c) #51321: strongly detached plasma. In (c) radiation layer moves close to the separatrix (see also fig. 3.54b lower trace).

emission was also seen to move, in the course of the transition from an attached to a detached plasma, from close to the target during the attached, to a position closer to the separatrix during the detached phase (fig. 3.60).

Difficult to understand are the rather low upstream temperatures $T_{eu}$ ~ 20 eV, measured with the edge Thomson scattering system at the inboard side in the triangular plane, i.e. toroidally in-between the divertor modules, which are very close to the measured downstream temperature $T_{ed}$ ~ 10 eV in the detached zones. More difficult to understand are these upstream temperatures in comparison to the observed downstream temperatures of $T_{ed}$ ~40 eV at the locations where the plasma remained attached (tile 5). One possible explanation for the observation could be an inhomogeneous temperature distribution at the separatrix and a MARF-like scenario. This point will be further investigated in the remaining experimental time of W7-AS.

The detachment not only helped to reduce the power load onto the divertor targets, but also led to a considerable reduction of the power losses due to line radiation from the plasma core. The cause of this is the, with rising density $<n_e>$, strongly falling impurity confinement time and the, at the low edge temperatures diminished impurity source due to reduced sputtering of high z impurities from the walls by CX neutrals. Whether also screening effects by the divertor plays a roll can not be concluded from the presently available experimental data.
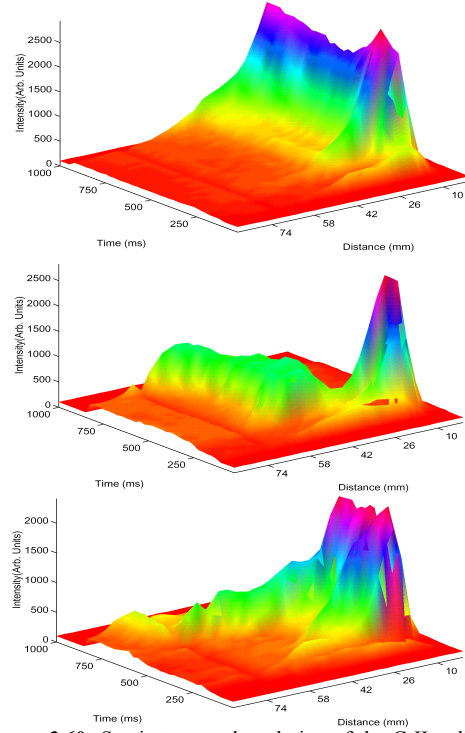
### 3.5.3.3 Comparison of 3-D transport modelling with first divertor experiments

A first attempt to model the island divertor experimental results with EMC3/EIRENE has been undertaken [Feng 2001a, Feng 2001b], albeit with closed magnetic islands which are about 30% smaller than the ones in the actual experiments. It is however believed that this does not affect the physics issues addressed in any considerable way. The calculations were done using nearly the same plasma parameters and transport coefficients as shown in fig. 2.16, except that the power has been decreased from 1 to 0.85 MW with increasing density until detachment occurs. The sputtering coefficient was fixed to 3% and $n_{eu}$ increased from

1-6 $10^{19}$ m$^{-3}$. Fig. 3.61 shows a comparison of the changes of $n_{ed}$ and of the normalised momentum loss with $n_{eu}$ with the experimental data from figure 3.58b. The nearly linear rise of $n_{ed}$ with $n_{eu}$ up to detachment confirm the previous predictions without impurities. The transition into detachment at $n_{eu}$=5.4 $10^{19}$ m$^{-3}$ results in a sharp drop in downstream density. Here a downstream temperature of 2 eV has been used, which is just about possible within the error margins. This low temperature leads to an inward shift of the ionisation zone for the neutrals and consequently to a drop of both the downstream density and the recycling flux. The code prediction that the island divertor plasma goes into detachment without



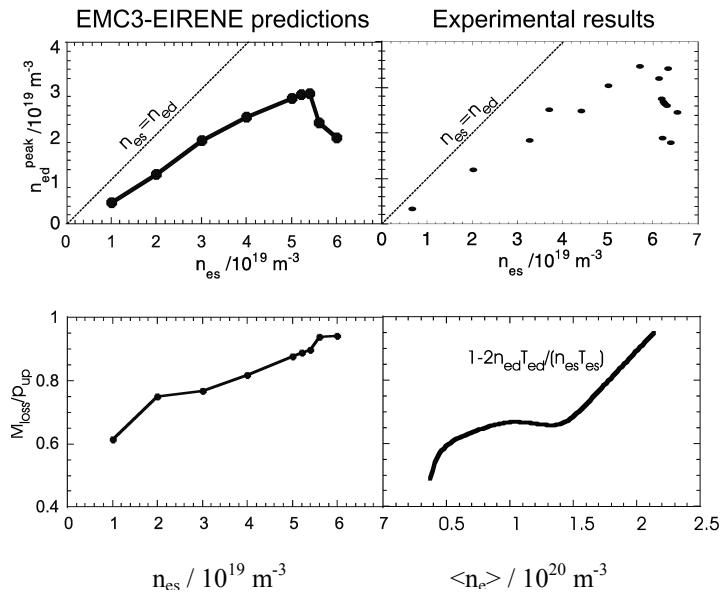**Figure 3.61:** Predicted and measured downstream densities and momentum loss factors as a function of the upstream density. The experimental downstream densities were taken from fig. 3.58b. The exp. momentum loss factors were derived for an earlier magnetic configuration (pulse #49748) [Grigull 20001a].
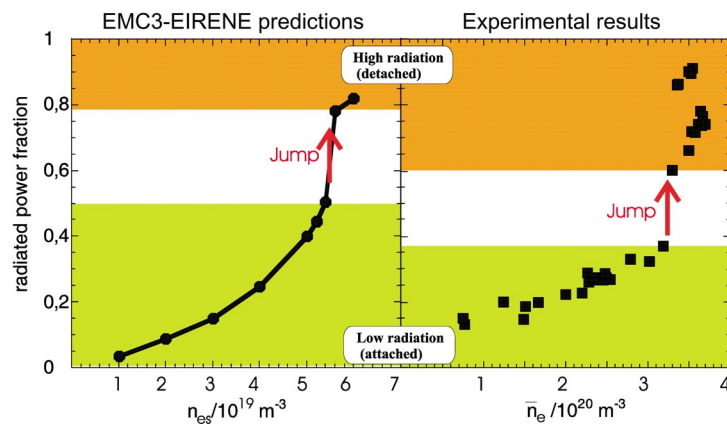


**Figure 3.62:** Predicted and observed jump of the carbon radiation at the detachment transition.

passing through the high recycling regime has clearly been confirmed by the experiments (fig. 3.61). In order to achieve attachment without high recycling high plasma densities are essential ($n_{eu}$=6 $10^{19}$ m$^{-3}$).

The cause for the lack of high recycling are the cross-field transport induced momentum loss processes discussed in chapter 2.2. The simulations in fig. 3.61c predicted strong momentum losses already at low densities and high temperatures, as has been observed in the experiments (fig. 3.61d)[Grigull 2001a]. It should be noted here that these measurements were performed in a configuration which was different from the one used for the other experiments reported on here (the data were taken before the 'optimum' configuration (fig. 3.50) had been found). A further prediction of the EMC3/EIRENE calculations, the jump of the carbon radiation layer at detachment, which had originally been found by a simple analysis of the global energy balance (see discussion in chapter 2.2), has also been experimentally verified by spectroscopic and bolometric measurements. It has so far been seen in all divertor discharges, that they can only either be run at a low radiation level of less than ~40 % of the absorbed power in an attached state or at high radiation levels of more than 60 % in the detached state (fig. 3.62).

## 3.6 W7-X

In W7-X, a large "advance stellarator" constructed of modular twisted superconducting coils will come into operation in 2006 (fig. 3.63). It can be operated with moderate shear and variable edge rotational transform in the range of $5/6 < \iota_a < 5/4$. The same island divertor concept as is presently being tested on W7-AS will be used on W7-X and the divertor will be implemented right from the start of operation. The standard configuration of W7-X ($\iota_a$=1=5/5) has five independent toroidally closed X-lines (fig. 3.64). Just as in W7-AS 10 open divertor modules will be installed in the elliptical planes (fig. 3.65), albeit actively cooled in order to accommodate
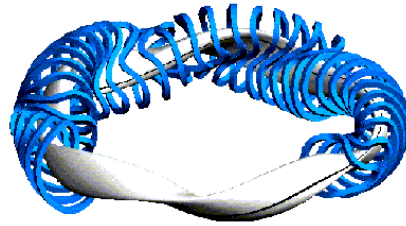


**Figure 3.63:** W7-X modular coil structure

long pulse discharges with $P_{ECRH}$=10MW and $P_{ICRH}$=4MW continuous operation (max. 30 min.) and $P_{NBI}$=5MW for several 10 sec intervals per 30 min discharge. The divertor modules will be made of CFC
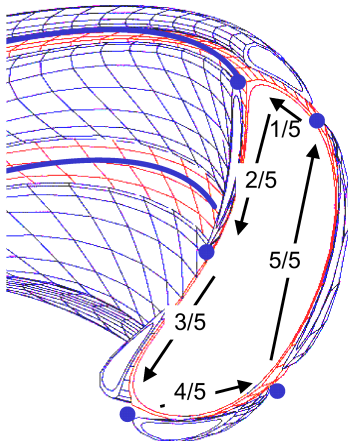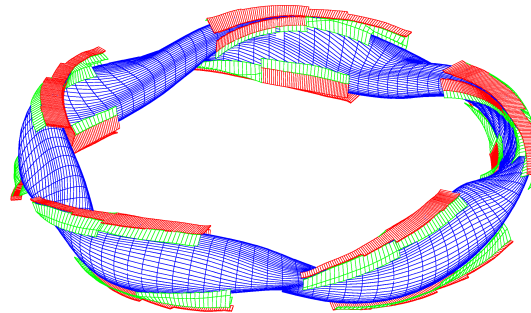


**Figure 3.64:** X-point and island locations around the main plasma at the elliptical plane.



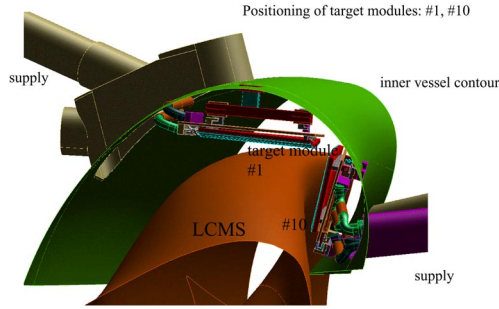**Figure 3.65:** Placement of the divertor modules. Red: targets, green: baffles

**Figure 3.66:** 3-D image of the installation of the horizontal and vertical targets and baffles inside the vessel.

in combination with a water cooled CuCrZr support (fig. 3.66). The open divertor construction can accommodate configurations from $\iota_a$= 0.7-1.25. The calculated expected power deposition patterns for the three main configurations, standard ($\iota_a$=1), low ($\iota_a$=5/6) and high $\iota_a$ ($\iota_a$=5/4) are shown in fig 3.67 Behind the targets (total surface area: 22 m$^2$ , wetted area: ~2 m$^2$, $[P/A]_{max}$=10 MW/m$^2$) and baffles (total surface area: 30 m$^2$, $[P/A]_{max}$=0.5 MW/m$^2$) cryo-pumps are installed. Additional control coils will be also installed in this machine to gain control over the important operational parameters connection length, island size and X-point height. They can also be used to compensate for symmetry breaking error fields. Further applications are sweeping (up to 20 Hz) of the strike points by 5 cm across the targets or to study ergodic effects.

A field line tracing code, with particle transport simulated by field line diffusion gave for an assumed transport coefficient of 1 m$^2$/s, a maximum power load on the targets of 8 MW/m$^2$ at full heating power. Calculations of the effect of <ß> with the new MFBE [Strumberger 1997] code have shown, that the divertor structure can safely handle the envisaged configurations at least up to <ß>=4% (fig. 3.67). Detailed studies of the 5/4 configuration, which is characterised by 5/4 island remnants embedded in a stochastic region outside the LCMS, have shown that the stochasticity increases with <ß>, but this does not pose any problems concerning the design of the divertor. 2-D B2/EIRENE calculations show a significant unloading of the target by radiation, especially when taking low-z impurities into account. The positioning of the pumping gap in the divertor modules and the geometry of the baffle plates was optimised by 3-D neutral particle studies with the EIRENE code [Reiter 1994].
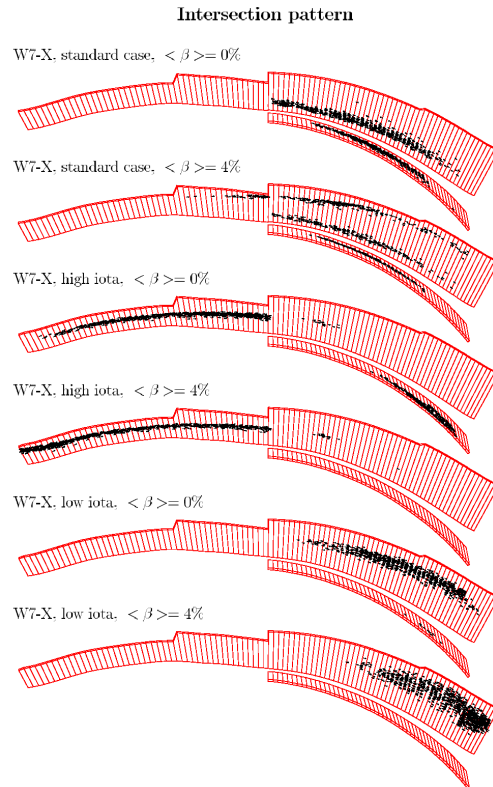


**Figure3.67:** Wetted areas on the divertor targets for the standard, high and low $\iota$ case and for different <ß> from field line diffusion calculations (D=1m$^2$/s).

## 4.     Summary and Conclusions

With the revival of the stellarator concept in the 1980's, following the experimental prove that plasma confinement in stellarators is equivalent to that in tokamaks, it was obvious that taking up the next step, from a medium sized to a large stellarator, would also mean that one would have to find solutions to the particle and power exhaust problem in these machines. This even more so, because with a new large machine, one would of course also want to demonstrate *the* major strength of the stellarator concept, it's steady state operation capability. Considerable theoretical and experimental efforts have therefore been undertaken in the last 10-15 years, in particular in Germany and Japan, which both decided to build a large stellarator respectively heliotron, to develop divertor concepts for the different types of stellarator lines followed at either location. Several promising solutions have been found, but could of course mostly only be studied in small short pulse machines.

The successful demonstration of  the principle suitability of the helical and local island divertor (LID) concepts on Heliotron E and CHS led directly to their implementation on LHD. The helical divertor concept, which is being developed towards a fully closed one in several steps on LHD, has already shown its principle suitability in the course of first experiments with an open actively cooled helical graphite tile structure, installed along the strike areas. The measured upstream and downstream plasma parameters clearly demonstrated the impact of collisions and viscosity for the long connection lengths on electron pressure. The non-linear increase in divertor pressure with rising core density is another promising result. The absolute values however were too small for efficient pumping due to the openness of the divertor structure, underlining the importance of the followed strategy, of stepwise approaching a carefully designed closed divertor structure. First experiments geared towards the full implementation of the first closed local divertor structure, the LID, planned for early next year, already demonstrated the successful creation of the necessary field structures. Hopes are high of course that the high pumping capability which this type of system already demonstrated on CHS can be revived. The fact that one recently succeeded in developing a RFLM field line mapping technique, which now allows to apply the far evolved 3-D EMC3/EIRENE transport code to configurations with arbitrary ergodicity, is a very promising development, which paves the way for detailed modelling of the divertor plasmas of helical devises like LHD in the near future. In a first step the code is being applied to the new TEXTOR-DED with its highly ergodic edge structure,  but it may as well also greatly foster the next steps in the development and design of the closed helical divertor structure of LHD.

The status of knowledge concerning the island divertor concept, which is the favoured concept for the modular 'advanced' stellarator lines, has reached already a fairly solid basis, in particular due to the experiments that have recently and are presently being performed with divertor modules very much alike those, that are under construction for W7-X . The results gained so far during the first few months of operation with a proper divertor modules were extremely encouraging, in that one succeeded immediately in running 'long' pulse, partially detached, quasi-steady state discharges which showed no signs of any limitations. Impurity confinement times were even found to drop sharply with increasing core density, while at the same time the energy confinement time was rising sharply in the newly accessible ultra high density (UHD) regime, to about twice ISS95. Moreover the measured divertor neutral pressures, were clearly sufficient for active particle pumping by

Ti gettering (this will be explored in due course on W7-AS) and of the same absolute value as would be required in W7-X. Radiative power fractions of up to 90% could be reached during detachment, with the radiation layer always remaining at the edge. During detachment the particle fluxes at the strike points dropped in the detached regions by factors of up to ~20, while at the remaining attached locations particle flux reductions between 1/3 and 3 were observed, i.e. the reduced fluxes at one location seem not to be taken over by other locations (this observation is further hardened by target tile calorimetry which covers most divertor locations) and the power load on the targets of the one module observed by a thermography camera was reduced by factors of about 4-16 for attached - detached regions.

A further area in which a great leap forward has been made is the code development. The latest version of EMC3/EIRENE with impurity transport now included, has already proven to be extremely valuable. A number of predictions, like the access to detachment without the necessity to go through a high recycling phase, because of island stellarator specific effects or the jump in the radiated power fraction at the detachment transitions, would have been hard to fully understand otherwise. Moreover the already found promising agreement between code predictions and first experimental results makes it quite likely that, after further benchmarking of the code in the course of the last experimental campaign of W7-AS, a very powerful tool will finally be available for the prediction of the behaviour of the W7-X divertor plasmas.

# 5.    References:

| | |
|---|---|
| [Boykov 1998] | Bykov V Ye, Chechkin V.V., et al., 25th EPS Conference on Controlled Fusion and Plasma Physics (Praha 1998), Vol **22C**, p. 464 |
| [Brakel 2000] | Brakel R., Summer University, Berlin, Sept. 2000 |
| [Braams 1986] | Braams B.J., Ph.D thesis, Rijksuniversiteit Utrecht 1986 |
| [Burhenn 1995] | R.Burhenn et al.,Proc. 22nd EPS Conf. on Contr. Fusion and Plasma Physics (Bournemouth) 19C Part III, 145 (1995) |
| [Burhenn 1997] | R.Burhenn et al. ,Proc. 24th EPS Conf. on Contr. Fusion and Plasma Physics (Berchtesgaden) 21A Part IV, 1609 (1997 |
| [Chechkin 1997] | Chechkin V.V., et al., 24th EPS Conference on Controlled Fusion and Plasma Physics (Berchtesgarden 1997), Vol **21A**, part IV, p. 901 |
| [Chechkin 2000] | Chechkin V.V., et al., Nucl. Fusion **40** (2000) 785 |
| [Feng 1997] | Feng Y. et al., J. Nucl. Mater. **241-243** (1997) 930 |
| [Feng 1999] | Feng Y., Kisslinger J., Sardei F., 26th EPS Conference on Controlled Fusion and Plasma Physics , Maastricht 1999, p4026 |
| [Feng 1999a] | Feng Y. et al., J. Nucl. Mater. **266-269** (1999) 812 |
| [Feng 1999b] | Feng Y., Kisslinger J., Sardei F., 12th Int. Stellarator Workshop, Madison, USA 1999 |
| [Feng 1999c] | Feng Y., Sardei F., Grigull P., et al., J. Nucl. Mater. **266-269**, 1928 (1999) |
| [Feng 2000] | Feng Y. and Kisslinger J., Contributions to Plasma Physics **40** (2000) 271 |
| [Feng 2001] | Feng Y., Sardei F., Grigull P, et al., 13th Int. Stellarator Workshop, Canbarra, Australia 2001 |
| [Feng 2001a] | Feng Y., Sardei F., Kisslinger J., Reiter D., Igitkhanov Y., 26th EPS Conference on Controlled Fusion and Plasma Physics , Madeira, Portugal (2001) |
| [Feng 2001b] | Feng Y., Kisslinger J., Sardei F., Reiter D., Igitkhanov Y., this conference |
| [Gardelmeier 2001] | Gardelmeier F., Feng Y., Grigull P., et al., 26th EPS Conference on Controlled Fusion and Plasma Physics , Madeira, Portugal (2001) |
| [Greenwald 1988] | Greenwald M., et al., Nuclear Fusion **28** (1988) 2199 |
| [Grigull 1997] | Grigull P., Hildebradt D., et al., J. Nucl. Mater. **241-243**, 935 (1997) |
| [Grigull 1999] | Grigull P., Hirsch M., McCormick K., et al., 26th EPS Conference on Controlled Fusion and Plasma Physics , Maastricht 1999, Vol. **23J** (1999) 1473 |
| [Grigull 2001] | Grigull P., McCormick K., et al., 26th EPS Conference on Controlled Fusion and Plasma Physics , Madeira, Portugal (2001) |
| [Grigull 2001a] | Grigull P., Kisslinger J., McCormick K., König R., et al., W7-X Divertor Symposion Greifswald, 2001 |
| [Herre 1998] | Herre G. et al., J. Nucl. Mater. **241-243** (1997) 941 |
| [Herre 1999] | Herre G. et al., J. Nucl. Mater. **266-269** (1999) 1015 |
| [Hofmann 1995] | Hofmann J.V., Das J., Grigull P., et al., 10th Intern. Stellarator Conference, Madrid, Spain, 1995 |
| [Iiyoshi 1999] | Iiyoshi A., Nucl. Fusion 39, 1245 (1999) |
| [Karger 1974] | Karger F., H. Wobig et al., Proc. 5th Int. Conf. on Fusion Energy, Tokyo 1974, IAEA, Vienna 1974, Vol. 1, 207 |
| [Karger 1977] | Karger F., K. Lackner, Phys. Lett. **61A** (1977) 385 |
| [Karger 1987] | Karger F., 14th EPS, Madrid 1987, Europhys. Conf. Abstracts 11D, post deadline paper |
| [Kisslinger] | Kisslinger J., private communication |
| [Komori 1994 ] | Komori A., Ohyabu N., et al., IAEA Seville 1994, Vol. 2, p 773, IAEA-CN-60/F-P4 |
| [Komori 1997] | Komori, J. Nucl. Mater. **241-243**, 967 (1997) |
| [Komori 1998] | Komori A., Fus. Eng. Des. **39-40**, (1998) 241 |
| [Komori 1998a] | Komori A., J. Plasma Fusion SERIES, Vol. **1**, (1998), 398 |
| [Komori 1999] | Komori A., Stellarator Workshop, Madison 1999 |
| [Komori 2001] | Komori A., Ohyabu N., Yamada H., et al., Physics Plasmas **8**, 2002 (2001); Progress of Large Helical Device Project 1989-1998 - Construction of LHD and Initial Experiments - NIFS |
| [König 2001] | König R.W.T., McCormick K., Feng Y., et al., ., J.Nucl. Mater. **290-293**, (2001) 882 |
| [Kubota 1998] | Kubota Y., Noda N., Inagaki S. et al., 20th SOFT Conference 1998, p. 241 |
| [Livshitz 1990] | Livshitz A.I., et al., J. Nucl. Mater. **170**, (1990) 79 |
| [Lyon 1997] | Lyon J.F., Klepper C.C., England A.C., 24th EPS CFPP 21A (1997) 777 |
| [Masuzaki 1997] | Masuzaki S., Komori A., et al., 24th EPS Conference on Controlled Fusion and Plasma Physics **21A** (1997) 821 |
| [Masuzaki 1998] | Masuzaki, J. Plasma Fusion Res. SERIES, Vol. **1**, (1998) 310 |

[Masuzaki 1999]     Masuzaki S.,Ohyabu N., Komori A., 26th EPS Conference on Controlled Fusion and Plasma Physics , Maastricht 1999, Vol**. 23J** (1999) 1345

[Masuzaki 2001]     Masuzaki S., J. Nucl. Mater. **290-293** (2001) 12

[Matsuura 1992]     Matsuura et al., NF **32**, 405 (1992)

[McCormick 1999]    McCormick K.,  P. Grigull, et al. , Plasma Phys. Contr. Fusion **41** (1999) B258

[McCormick 1999]    McCormick K., Grigull P., Baldzuhn J., et al., et al., Plasma Phys. Control. Fusion, **41**, B285 (1999)

[McCormick 2001]    McCormick K., Grigull P., König R., et al., J.Nucl. Mater. **290-293**, (2001) 920

[McCormick 2001a]   McCormick K., Grigull P., Ehmler H., et al., 26th EPS Conference on Controlled Fusion and Plasma Physics , Madeira, Portugal (2001)

 [Mizuuchi 1991]     Mizuuchi et al., 18th EPS Conference, Berlin 1991, Vol. 5C, Part III, p.65

[Mizuuchi 1999]     Mizuuchi, 12th Int. Stellarator Workshop, Madison (1999)

[Mizuuchi 2001]     Mizuuchi, J.Nucl. Mater. **290-293**, (2001) 678

[Morisaki 1997]     Morisaki, J. Nucl. Mater. **241-243**, 977 (1997)

[Motojima 1984]     Motojima, J. Nucl. Mater. **128 & 129**, 524 (1984)

[Niedermeyer 2000]  priv. communications

[Nishimura 2001]    Nishimura K., Stellarator News **75**, May 2001

[Noda 2001]         Noda N., W7-X Divertor Symposion Greifswald, 2001

[Obiki 1988]        Obiki et al. IAEA '88, Plasma Physics and Controlled Fusion, p.337, IAEA-CN-50/C-I-1

[Obiki 1990]        Obiki et al., Fus. Techn. **17**, 101 (1990)

[Obiki 1999]        Obiki T., et al., 12th Int. Stellarator Workshop, Madison (1999)

[Obiki 2000]        Obiki T., et al., 18th IAEA Fusion Energy Conference, Sorento, Italy (2000), IAEA-CN-77/Exp1/09

[Ohyabu 1992]       Ohyabu N., J. Nucl. Mater. **196-198** (1992) 276

[Ohyabu 1993]       Ohyabu N., et al., Plasma Phys. Contr. Fusion Research, (Proc. 14th Int. Conf. Würzburg, 1992), Vol. 2, IAEA, Vienna (1993) 605

[Ohyabu 1994a]      Ohyabu N., Nucl. Fus. **34**, 387 (1994)

[Ohyabu 1995]       Ohyabu N., J. Nucl. Mater. **220-222** (1995) 298

[Ohyabu  1998]      Oyabu N., J. Plasma Fusion SERIES, Vol. **1**, (1998), 135

[Ohyabu 1999]       Ohyabu N., J. Nucl. Mater. **266-269** (1999) 302

[Ohyabu 2000]       Ohyabu, N., Phys. Rev. Lett. **84**, 103 (2000)

[Ohyabu 2001]       Ohyabu, N., W7-X Divertor Symposion Greifswald, 2001

[Peterson 2001]     Peterson B.J., Nakamura Y., Yamasaki K., et al., Nucl. Fus. **41** (2001) 519

[Reiter 1984]       Reiter D., Jülich Report 1947, Jülich

[Sagara 1995]       Sagara A., Ohyabu N., Suzuki H., Motojima O., J. Nucl. Mater. **220-222** (1995) 627

[Sardei 1994]       Sardei F., Contrib. Plasma Phys. **34**, 113 (1994)

[Sardei 1997]       Sardei F. et al., J. Nucl. Mat. **241-243** (1997) 135

[Sardei 1997]       Sardei F., Feng Y., Grigull P., et al., J. Nucl. Mater. **241-243**, 135 (1997)

[Sardei 2001]       Sardei F., Feng Y., Kisslinger  J., W7-X Divertor Symposion, Greifswald, Germany 2001

[Stroth 1996]       U. Stroth et al., Nucl. Fusion **36**, 8 (1996) 1063-1077

[Strumberger 1997]  Strumberger E., IPP-report 2/339 (1997)

[Strumberger 1999]  Strumberger E., J. Nucl. Mat. **266-269** (1999) 1207

[Takase 1994]       Takase H., Ohyabu N., Nucl. Fus. **35**, (1994) 123

[Wenzel 2001]       this conference

[Wobig 1987]        Wobig H., Z. Naturforsch. **42a** (1987) 1054

[Zushi 1996]        Zushi H., Mizuuchi T., Nagasaki K.,  et al., Plasma Physics and Controlled Fusion **38** (1996) 1307